ARTICLES
https://doi.org/10.1038/s41560-020-00770-w

nature energy

Elastocaloric heat pump with specific cooling power of 20.9 W g^{-1} exploiting snap-through instability and strain-induced crystallization

F. Greibich[1,2], R. Schwödiauer[1,2], G. Mao[2], D. Wirthl[1,2], M. Drack[1,2], R. Baumgartner[1], A. Kogler[1], J. Stadlbauer[1,2], S. Bauer[1,3], N. Arnold[1,2] and M. Kaltenbrunner[1,2] ✉

Conventional refrigeration relies on hazardous agents, contributing to global warming. Soft, cheap, biodegradable solid-state elastocaloric cooling based on natural rubber offers an environmentally friendly alternative. However, no such practical cooler has been developed, as conventional soft elastocaloric designs are not fast enough to ensure adiabaticity. Here, we combine snap-through instability with strain-induced crystallization and achieve a sub-100 ms quasi-adiabatic cycling, which is 30 times faster than previous designs. Negligible heat exchange in expansion/contraction stages combined with the latent heat of phase transitions results in a giant elastocaloric crystallization effect. The rubber-based all-soft heat pump enables a specific cooling power of 20.9 W g^{-1}, a heat flux of 256 mW cm^{-2}, a coefficient of performance of 4.7 and a single-stage temperature span between hot and cold reservoirs of 7.9 K (full adiabatic temperature change of rubber membrane exceeding 23 K). The pump permits a compact all-soft voltage-actuated set-up, opening up the opportunity of a viable plug-in-ready cooling device.

A substancial fraction of the world's cooling demand is provided by vapour-compression refrigeration systems. This technology depends on hazardous gases and cooling fluids with high global warming potential and consumes large amounts of electricity often generated from fossil fuels[1,2]. Even though more environmentally friendly vapour refrigerants have been developed, such as hydrocarbons, hydrofluoric olefins and carbon dioxide, many restrictions still have to be balanced in applications, including long-term impact on the environment, cost, efficiency, space and safety[2–5]. This calls for the development of more efficient and greenhouse-gas-free systems, which are cheap enough to be employed on a global scale.

Solid-state cooling based on different caloric effects (magneto-, electro-, baro- and elastocaloric) is a promising technology to fulfil these requirements and offers an environmentally friendly, efficient and economic solution[6–10]. Mechanocaloric materials, in particular colossal barocaloric and elastocaloric materials, together with giant electrocaloric and magnetocaloric designs are expected to replace harmful fluids in refrigeration and heat pumping technologies[7]. The elastocaloric effect, in particular, has been identified as the most promising alternative by the US Department of Energy[7,11]. However, the majority of devices developed so far raise a number of new environmental concerns. Magnetocaloric cooling is the most developed of all caloric solid-state technologies[10]. State of the art devices reach efficiencies competitive with vapour-compression refrigeration systems and are at the brink of market introduction[6–9]. The materials used, especially the permanent magnets, contain large amounts of rare earth metals, which require a high energy expenditure in production and leave behind considerable amounts of toxic waste. Additionally, they are expensive, and supply security is subject to considerable geopolitical risks[6].

The electrocaloric effect is still in its infancy; furthermore, most electrocaloric materials contain lead, rendering them unsustainable. Polyvinylidene-fluoride-based polymers and $BaTiO_3$ were identified as environmentally friendly alternatives, but only a few functioning devices have been reported to date[6]. Electrostatically actuated electrocaloric cooling devices based on polyvinylidene fluoride[12] show a high coefficient of performance (COP); however, the high cost of polyvinylidene fluoride hampers large-scale market penetration. The colossal barocaloric effects in plastic crystals open up possibilities with high entropy changes and an adiabatic temperature change ΔT of 50 K (refs. [13,14]), but the required pressure variations are hundreds of MPa, and a practical application is still far away. For elastocaloric devices, NiTi-based alloys are the most prominent active material. NiTi-based alloys exhibit a large elastocaloric effect with an isothermal entropy change ΔS of 35.1 J kg^{-1} K^{-1}, with the largest ΔT of 40 K resulting from an austenite–martensite phase transformation[15,16]. Several prototypes have been reported[6,17], including one using thin-walled NiTi tubes under compression[18] that reaches a maximum ΔT of 27 K at large strains and has a small-strain COP above 20 and a highest specific cooling power (SCP) of 18 W g^{-1}, achieved by fast heat transfer and high operation frequency in a miniature-scale device[19]. However, the large forces required for operation pose a major engineering challenge; the stress required to drive NiTi shape memory alloys is as high as 700 MPa (ref. [20]), making scale-up difficult. Some of the NiTi shape memory alloys demonstrate a maximum adiabatic temperature change as high as 31.5 K (ref. [21]) and COP in the range of 3.5–20, as well as practically unlimited lifetime in moderate-strain cycling compression[18]. The large-strain fatigue-life of such elastocaloric materials[9,20,22], typically a few thousand cycles[8], may nonetheless be a limiting factor when large temperature spans and/or tensile cycling are required.

The current focus on shape memory alloys overshadows a promising class of materials with an exceptionally strong elastocaloric effect at room temperature: elastomers such as natural rubber (NR)[6,12,23]. Contrary to most caloric materials, NR is soft, cheap and

---

[1]Division of Soft Matter Physics, Institute for Experimental Physics, Johannes Kepler University Linz, Linz, Austria. [2]Soft Materials Lab, Linz Institute of Technology, Johannes Kepler University Linz, Linz, Austria. [3]Deceased. ✉e-mail: martin.kaltenbrunner@jku.at

biodegradable, simultaneously solving some of the major engineering and sustainability issues of artificial cooling. The wide availability of NR, together with the low mechanical forces required for stretching, make it an ideal candidate for future large-scale, high-power cooling devices.

Constructing an elastomer heat pump that enables cooling is challenging, and attempts to build one are rare. The elastocaloric effect of NR was explored to build elastomer heat engines for classroom purposes early on[24–26], with theoretical description following later[27,28]. The US National Aeronautics and Space Administration (NASA) patented a design for a manually operated device for use in space emergencies[29]. A design based on uniaxial deformation of rubber stripes with a crankshaft was tested, but no cooling effect was achieved due to poor heat transfer and large frictional heating[30]. More recently, a regenerative heat pump was developed[31], which uses oscillatory stretching of a NR pipe with an oscillating fluid flow through it and an externally superimposed axial temperature gradient. The rubber is not adiabatic in this set-up, as thermal contact with the fluid is permanent and the stretching rate is low.

Here we propose a heat pump design to solve these issues and demonstrate a functioning elastomer-based cooling system. It combines strain-induced crystallization (SIC)[32,33] of NR with snap-through instability[34,35], resulting in sub-100 ms quasi-adiabatic actuation 30 times faster than in conventional set-ups. This produces what we call a giant elastocaloric crystallization (geCC) effect, which includes entropy-elastic and SIC contributions[6,23]. In brief, stretching rubber aligns its randomly coiled molecular chains, lowering the number of possible conformations. For adiabatic deformation, such a decrease in conformational entropy S_{config} increases the thermal entropy S_{thermal}, that is, heats the material. This process is reversible, and the initial state is recovered upon relaxation. Strong stretching also leads to a partial transformation of the NR molecules into an ordered crystallized phase accompanied by the release of latent heat. This phase transition, too, is reversible to a high degree[23]. Of these two effects (schematically illustrated in Fig. 1a), the SIC-related heating is dominant, which yields a high SCP that exceeds other approaches[4,12,19,36–42] (Fig. 1e and Supplementary Table 1). Using voltage-controlled elastomer actuation[35], we also open up a path towards a plug-in-ready all-soft heat pump.

Operational principle and set-up

We develop a set-up, based on balloon inflation, with almost equal biaxial stretch, inherently efficient heat transfer and no frictional losses, far superior to uniaxial stretch designs. Infrared measurements (Fig. 1b,c and Supplementary Video 1) verify the temperature increase of the NR during the inflation (state 2), the temperature equilibration with the surroundings (states 1 and 3) and the temperature decrease upon deflation (state 4)[34,43]. Figure 1d shows the operating principle of our geCC device; further details on the experimental set-up are given in the Methods in the section 'Experimental realization of the geCC heat pump' and Supplementary Fig. 1. The active material is a thin latex membrane mounted onto a pressure vessel by a clamp with a central circular aperture. In the first step ($1 \rightarrow 2$) the membrane is stretched during fast adiabatic inflation into a balloon, which leads to an increase in temperature. In the second step ($2 \rightarrow 3$) the membrane exchanges heat with the high temperature reservoir (HTR). The HTR consists of an aluminium cylinder with a concave spheroidal cavity that precisely fits the shape of the inflated balloon. We varied the maximum stretch of the membrane using a small ($\mathrm{HTR_S}$) and a large ($\mathrm{HTR_L}$) version of this reservoir. In the third ($3 \rightarrow 4$) and fourth ($4 \rightarrow 1$) steps the membrane contracts adiabatically and thus cools, followed by heat absorption from the low temperature reservoir (LTR). The LTR is an aluminium spherical cap with a mass of 1.9 g. This operational cycle possesses several major advantages. First, the nearly spherical geometry of the pressurized balloon ensures efficient heat transfer, as the internal overpressure intrinsically applies a contact force perpendicular to the surface of the heat sink. Second, friction and the associated dissipation and heating are reduced to a minimum, because the contact between the membrane and the heat reservoirs remains static during the heat exchange. This, in conjunction with the small thickness and weight of the NR membrane, results in a SCP of 20.9 W g^{-1}, outperforming other elastocaloric cooling devices (Fig. 1e and Supplementary Table 1). Third, to minimize the impact of parasitic heat exchange with the surroundings (to ensure adiabaticity), strain rates need to be high. Pressure-driven actuation of a rubber membrane realizes quasi-instant stretching (within ~100 ms, area strain rates of 16,000% s^{-1}) by exploiting the snap-through instability[35].

This mechanical snap-through instability is observed for elastomer balloons with low viscoelasticity and can be theoretically described by constitutive models with stiffening, for example, the hyperelastic Gent model for rubber[44]. We discuss the pressure–volume ($p-V$) diagram of one inflation–deflation cycle with volume constraints (as imposed by the LTR and HTR) schematically (Fig. 2a) and compare it with the experimental data (Fig. 2b). At the onset (A), pressure rises steeply, while volume change remains minimal. When the pressure reaches the value p_{B} (B), the snap-through instability causes a rapid expansion of the balloon to the limiting volume determined by the HTR (C). Decrease in internal overpressure (D) leads to a similarly swift jump (E,F) towards the initial size (determined by the LTR). The hysteresis in the $p-V$ diagram is to a large extent caused by the SIC[23,33,45] (Supplementary Note 2 and Supplementary Fig. 2). Due to different dynamics of crystallization and melting, the crystalline fraction for a given strain is higher during contraction (schematically shown in Fig. 2c)[32,33,45–47]. The stress is lower there, because the extended crystallized parts of the chains allow the remaining amorphous fraction to relax (illustrated in Fig. 2c). The area enclosed by the $p-V$ diagram represents the mechanical input energy, used in COP and SCP calculation (equations (22)–(24) in Supplementary Note 3). Measurements yielded 0.09 J ($\mathrm{HTR_S}$) and 0.31 J ($\mathrm{HTR_L}$) per cycle (Supplementary Fig. 3). Due to the high crack-growth resistance of the crystalline phase, SIC also improves membrane fatigue properties. Though cyclic operation in the SIC regime (prestretch > 200%) allows for lifetimes of ~10^7 cycles, which fulfils the requirement for commercial applications[6], our demonstrative device operates partly in the fully amorphous range, resulting in a shorter lifetime (~10^3 cycles; Supplementary Video 2). However, since SIC provides the main contribution to the cooling power, there is a large potential for increasing lifetime and enhancing device performance[6]. The temperature–entropy ($T-S$) diagram in Fig. 2d represents a reversed Otto cycle for the membrane. It contains a SIC phase change and highlights the thermal aspects of the elastomeric heat pump. In contrast to a Rankine cycle[48], which is used in the majority of steam turbines and refrigerators, the heat exchange here happens at constant stretch, not pressure (stress).

Thermodynamics of heat pump cycle with crystallization

In conventional elasticity of purely amorphous rubber, the entropy (density) of the elastomer additively separates into a purely configurational term S_{config}, which depends on stretch λ, and a purely temperature-dependent term S_{thermal}:

$$S = S_{\mathrm{config}}(\lambda) + S_{\mathrm{thermal}}(T) \tag{1}$$

In the presence of SIC, the expression for the entropy is more complicated (equation (1) in Supplementary Note 1):

$$S = -\chi \frac{U_{\mathrm{ac}}}{T_{\mathrm{c},0}} + S_{\mathrm{ch}}[\lambda, \chi] + c \ln \frac{T}{T_S} \tag{2}$$

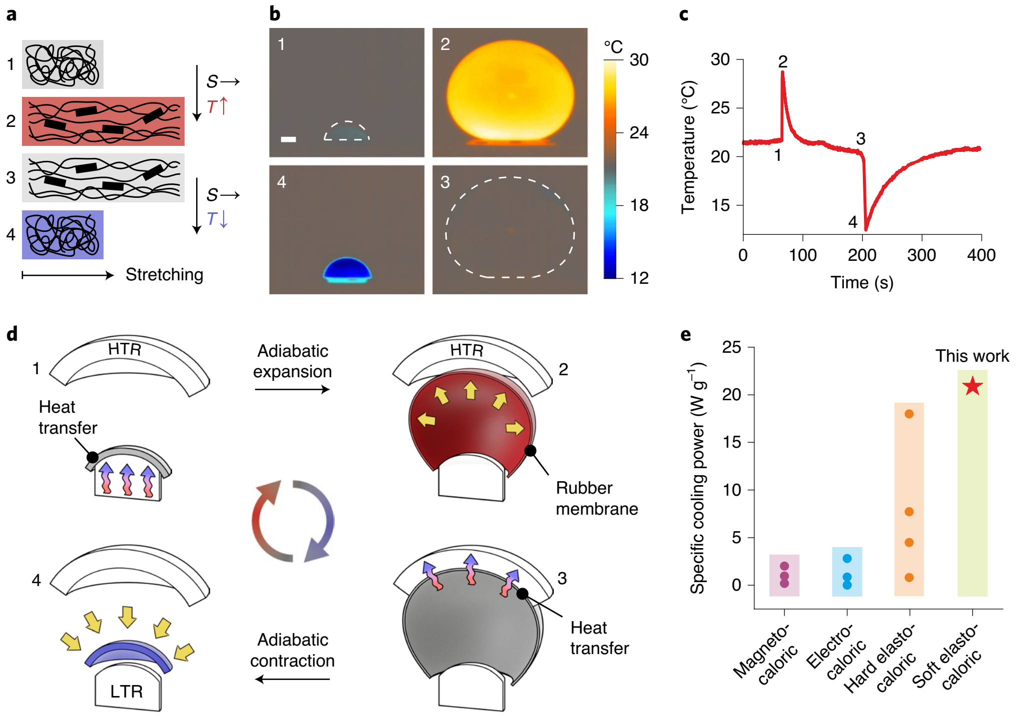

Fig. 1 | Illustration of the geCC effect in elastomers, heat pump design principle and performance comparison. a, Ordering of coil-like molecular chains and strain-induced crystallization (black rectangles) in an adiabatic stretching (1–2) and contraction (3–4) leads to release/absorption of heat and reversible heating (red) and cooling (blue). The direction of changes in entropy S and temperature T is indicated by arrows behind the corresponding symbols. States of the system are the same in **a**–**d**, and the change in size is indicated by black arrows in **a** and **d**. **b**, Infrared images of rapid membrane inflation and deflation showing the deformation-induced temperature changes. After both deformation steps, the membrane temperature is allowed to equilibrate with the surroundings and is poorly visible. It is indicated by the dashed lines in sub-panels 1 and 3. Scale bar, 1 cm. **c**, Temporal behaviour of membrane temperature, deduced from infrared images similar to those in **b**. **d**, To utilize the geCC effect in a heat pump, a cooling target (LTR) is placed beneath the membrane. The HTR further accelerates heat exchange with the surroundings. **e**, The SCP of our device surpasses that of other solid-state cooling systems[4,12,19,36–42]. Individual dots refer to different set-ups, grouped into bars for various classes (Supplementary Table 1).

The first term reflects the decrease in configurational entropy due to the crystallization of individual structural units, where χ is the crystalline fraction, U_{ac} is the latent heat of crystallization per unit volume and $T_{c,0}$ is the unstretched crystallization temperature. The second term describes the configurational entropy of the partially crystallized chains (S_{ch}, roughly equivalent to S_{config} in equation (1)), and the third term gives the thermal contribution, c being the volumetric heat capacity and T_S some universal reference temperature. To obtain the adiabatic stretch–temperature relation, one has to compute the equilibrium entropy $S_{eq}(T,\lambda)$ and free energy $F_{eq}(T,\lambda)$ by substituting $\chi=\chi_{eq}(T,\lambda)$ from the equilibrium condition (equations (3)–(6) in Supplementary Note 1 for the detailed derivation):

$$cdT = U_{ac}d\chi + s\left[T,\lambda,\chi_{eq}(T,\lambda)\right]d\lambda \tag{3}$$

Here $s=\frac{\partial F_{eq}(T,\lambda)}{\partial\lambda}$ is the (equilibrium nominal, one dimensional) stress for a given temperature and stretch. Our thermodynamic cycle consists of two adiabats (expansion and contraction) and two iso-strain curves, where the heat exchange with LTR and HTR takes place.

In the adiabatic processes AC and DF ($dS=0$, see Fig. 2d) the change in total configurational entropy (first two terms on the right hand side in equation (2)) is balanced by the opposite change in thermal entropy. Expansion reduces and contraction increases the configurational entropy of the chains. Additionally, an entropy change of structural units upon SIC/amorphization is released/absorbed as latent heat, amplifying the change in membrane temperature (Fig. 3a–d and Supplementary Video 3). This is quantified by equation (3), reflecting the adiabatic energy balance, because the internal energy is $U=cT-\chi U_{ac}$. The simplicity of equation (3) is misleading, as it implies the knowledge of the function $\chi=\chi_{eq}(T,\lambda)$, but both stretching and crystallization increase the temperature. The adiabatic temperature change depends on the maximum stretch defined by the HTR size (end of Supplementary Note 2, the Methods in the section 'Infrared temperature measurements of NR membranes', Fig. 3e and Supplementary Note 9); as expected, the cooling of the LTR is larger and faster for the HTR_L with a larger stretch (Fig. 2e).

During the heat exchanges CD and FA (Fig. 2d), the stretch λ remains constant ($d\lambda=0$), therefore the stress s performs no work ($sd\lambda=0$), and the energy balance similar to equation (3) reads $TdS=dU=cdT-U_{ac}d\chi$. As χ_{eq} decreases with T, the right hand side here increases with T. Thus, the total entropy also increases, and the slope of both iso-stretch legs in Fig. 2d is positive. The fully amorphous FA leg is steeper than segment CD on the HTR (a thin line with χ is shown for comparison), because changes in χ are opposite to changes in T and S there. During cooling, χ increases, and latent heat diminishes the temperature drop. The highest crystallinity in a cycle is reached after cooling on the HTR, and the adiabatic temperature drop DF (Fig. 2d) is larger than the AC increase. The thermal entropy always follows the temperature changes. The first entropy term in equation (2) also increases with T, due to a decrease in $\chi_{eq}(T)$ for $\lambda=$const. The behaviour of the second, chain term can be understood from the equilibrium condition (equation (2) in Supplementary Note 1). It turns out that S_{ch} increases with χ (for a fixed λ), while the total S_{config} (sum of the first and second terms) decreases with it.

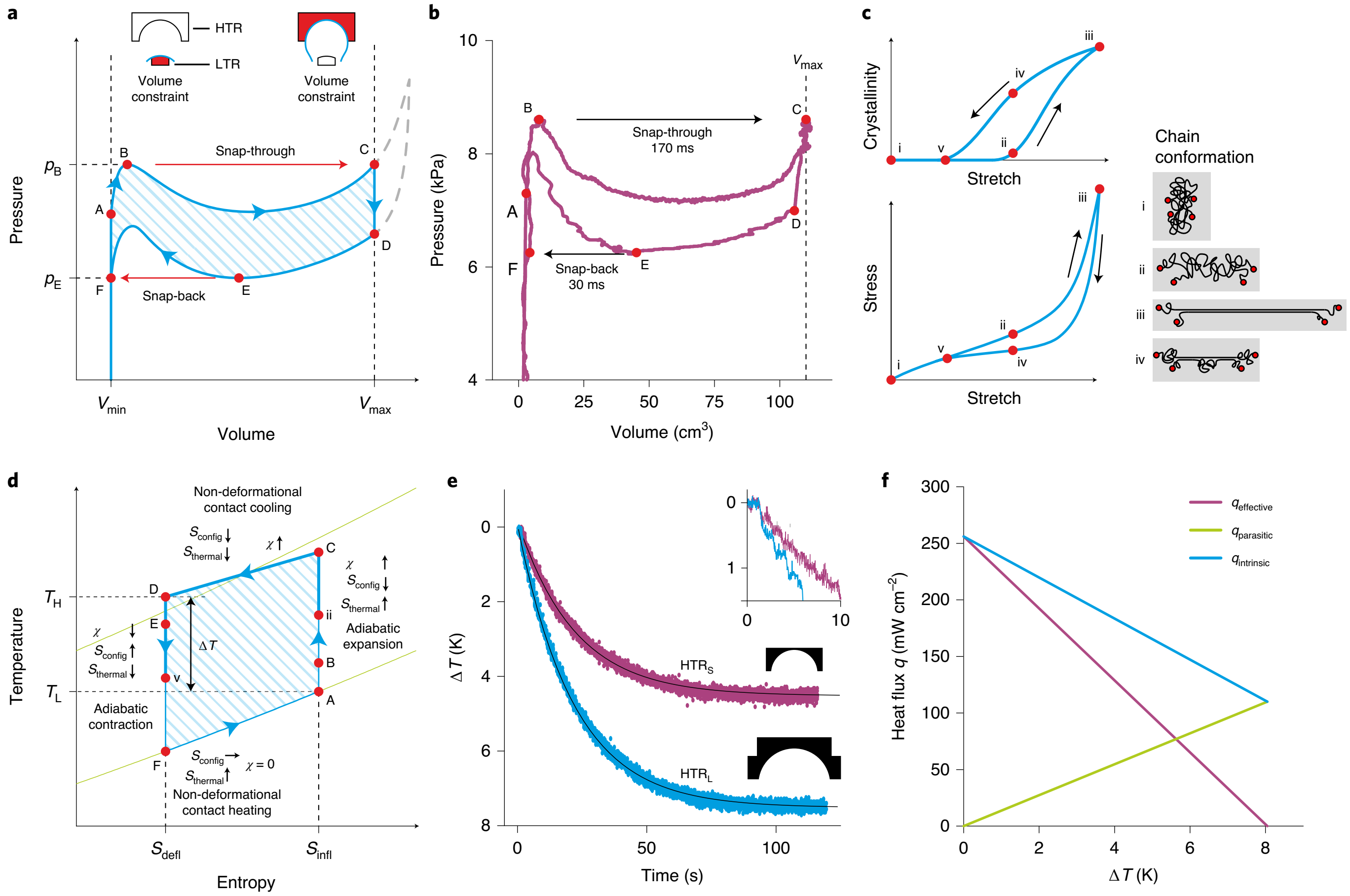

Fig. 2 | Elastic and thermal properties of a NR membrane and resulting cooling performance of the heat pump. a,**b**, Theoretical and measured *p*–*V* diagram of one actuation cycle with 140 μm membrane and HTR$_S$. BC and EF indicate the adiabatic snap-through and snap-back (initiated at the corresponding pressures p_B and p_E) with the measured snapping times (the whole deflation leg DEF lasts 80 ms), while CD and FA represent the heat exchange with the HTR and LTR (inset). The letters correspond to those used in the *T*–*S* diagram of the cycle in **d**, and the hatched area in **a** and **d** corresponds to the work performed in a cycle. **c**, Schematic illustration of crystallization and hysteresis in the stress–stretch relation for NR. The sample starts from the unstretched state (i) with fully amorphous coiled chain conformations, and moves towards a state of maximum crystallinity (around 25%; iii), where an appreciable fraction of chains is aligned along the stretch direction (in the one-dimensional case), as schematically indicated. For a given stretch, the crystallinity during expansion (ii) is always lower than for relaxation (iv), where it vanishes at a lower stretch (v), resulting in a different elastic response for both stages. **d**, *T*–*S* diagram of the refrigerating Otto cycle with phase change. The idealized cycle (blue tetragon) is constrained by the iso-strain *T*(*S*) curves of the membrane (green) and adiabats. Thicker lines between points ii and v (see panel **c**) indicate parts of the cycle where crystallinity is present. T_H and T_L indicate the temperature of the HTR and LTR, respectively. S_{defl} and S_{infl} denote the constant entropies during the adiabatic deflation and inflation of the membrane. **e**, Measured multi-cycle cooling curves of the LTR (purple and blue lines) with corresponding fits by the exponential equation (12) in Supplementary Note 3 (black lines) for the small (S) as well as large (L) HTR with 140 μm membrane at 1.1 Hz. The inset shows individual cycles at the initial stage of cooling for the small and large HTR. The shape of the used HTR is indicated next to the cooling curve. **f**, Estimation of the parasitic heat flow $q_{parasitic}$ for the LTR (green line), which leads to a deviation of the measured ideal, intrinsic heat flow ($q_{intrinsic}$, averaged over cycles, blue line) from the effective heat flow ($q_{effective}$, purple line). Here we used a 180 μm membrane on HTR$_L$ at 1.1 Hz.

Figures of merit in a multi-cycle operation

In our set-up, the HTR remains at room temperature, as its heat capacity is more than 100 times larger than that of the LTR and over 1,000 times larger than that of an elastomer membrane. We measure temperature curves of the LTR at different cycle frequencies, maximum stretches and membrane thicknesses. The heat pump characteristics COP and SCP are then determined from the time constants and the final temperatures of these curves in relation to the ideal, intrinsic membrane temperature changes (see Supplementary Note 3, particularly the final result in equations (22)–(24)). For quantification, we use the onset of the temperature curve, because later (for $\Delta T < 0$), parasitic heat exchange with the surroundings diminishes measured values. However, we can estimate the impact of parasitic heat, as shown in Fig. 2f (also Supplementary Fig. 4). The results for different parameters are summarized in Table 1.

The highest COP of 4.7 is achieved for a 140 μm membrane with HTR$_S$ at 0.5 Hz. A larger frequency of 0.9 Hz moderately reduces COP, almost doubling the SCP to 10 W g^{-1}, while ΔT has its maximum HTR$_S$ value of 4.6 K. HTR$_S$ operation is highly efficient, because it limits the membrane expansion at the endpoint of the snap-through instability. Larger HTR$_L$ increases the SCP and ΔT, at the cost of reducing COP, presumably because the crystallinity saturates at high stretches[23]. Here, 0.9 Hz produces an SCP of 15.9 W g^{-1} and a ΔT of 6.8 K. The maximum SCP of 20.9 W g^{-1} is obtained at 1.1 Hz, for a slightly modified set-up (with 0.3-second-long pressure pulses of 6 bar).

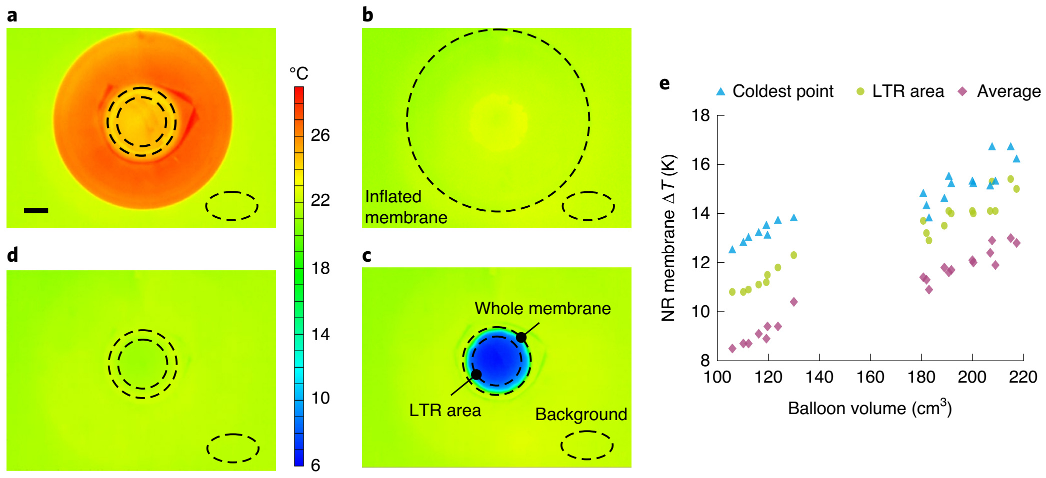

Fig. 3 | Adiabatic snap-back cooling. a, The balloon immediately after the fast inflation to about 200 cm^3. Infrared readings underestimate the quasi-adiabatic temperature increase, because the membrane is thin and semitransparent. The dashed oval indicates the background and the dashed circles indicate the initial relaxed membrane and the part of it that comes in contact with the LTR (see panel **c**). The bottom part of the balloon with the clamp set-up can be seen in this region. **b**, Inflated membrane, thermalized with the surroundings, right before the fast deflation. **c**, Fully relaxed membrane immediately after the fast, adiabatic snap-back contraction. The time difference between the adjacent frames, **b** and **c**, is 267 ms. The membrane is colder in the area that lies on the LTR in cycling experiments, and even colder in the very centre (panel **e**). **d**, Contracted membrane after the thermal equilibration with the surroundings, which proceeds much slower in these infrared measurements, as there is no LTR or HTR present. All frames are from Supplementary Video 3; temperature colour coding and scale is common for **a**–**d**. Scale bar, 1 cm. **e**, Intrinsic temperature changes of the membrane upon deflation, measured with the infrared camera, as described in the text. The measurements were performed for the expansion volumes close to the balloons on HTR$_S$ and HTR$_L$. Magenta diamonds, the average temperature change ΔT_{av} for the whole membrane, used for crystallinity estimations in equation (10) in Supplementary Note 1. Green circles, the changes for the part of membrane in contact with the LTR (panel **c**), ΔT_{mem}, used for the heat transfer calculations in equations (11)–(26) in Supplementary Note 3. The ΔT_{av} and ΔT_{mem} values used in calculations were obtained by extrapolation for the volumes 115 and 200 cm^3 in both cases. Blue triangles, the maximum observed temperature change in the very centre of the membrane. The full inflation–deflation adiabatic temperature change exceeds 23 K.

Table 1 | Summary of the experimental results for different parameters

Thickness, *H* (μm)	**Frequency, *f* (Hz)**	**Final LTR, ΔT_{meas} (K)**	**COP**	**SCP (W g^{-1})**	**Heat flux, *q* (mW cm^{-2})**
140	0.9	4.6	4.5	10.0	104
140	0.5	4.3	4.7	5.4	63
140	1.1	7.0	1.0[a]	20.9	205
140	0.9	6.8	1.9	15.9	156
180	1.1	7.9	0.9[a]	19.2	256
180	0.9	7.9	0.7[a]	15.6	222

[a] These values are smaller due to larger outlet diameter, as explained in Supplementary Note 8.

A thicker 180 μm membrane produces the highest ΔT of 7.9 K and heat flux of 256 mW cm^{-2} (Fig. 2f, Supplementary Fig. 4a,b and the discussion at the end of Supplementary Note 3); this flux value is much higher than that reported for other solid-state cooling devices[4,12]. The corresponding total flux, with the LTR area from Supplementary Note 9, is 877 mW. In our set-up, the LTR covers only ~45% of the aperture area, leaving considerable potential for increasing heat transport without altering mechanical input energy. Simulations indicate a possible improvement of heat pump performance by up to a factor of two (Supplementary Fig. 5 and Supplementary Note 4).

The operational longevity should further increase using working membranes from high-quality rubbers, custom precast into an almost spherical initial shape, operating in a narrower stretch range. This would reduce the harmful influences of stretch inhomogeneity, amorphous (non-SIC) stretch region and defects present in our commercial off-the-shelve samples (Supplementary Fig. 6). These factors decrease cycling lifetime, as discussed in Supplementary Note 6 and Supplementary Fig. 7. Furthermore, the full inflation–deflation adiabatic temperature change of our membrane working body exceeds 23 K (Fig. 3a,c and Supplementary Video 3). Therefore, the LTR temperature difference of 7.9 K reached in our set-up can potentially be more than doubled with the outlined improvements and optimization.

Our lab-scale demonstrator set-up is designed to determine all relevant performance parameters. A feasible practical device remains conceptually similar: it requires a LTR, a HTR, a membrane and a pressure vessel with a volume 5 to 10 times larger than the volume V_b of the inflated balloon on the HTR. For practical cooling applications, the LTR can be connected with a regenerative fluidic heat exchanger. The pressure transducer can be a conventional linear or rotational piston transducer, a voltage-controlled elastomer actuator (discussed in the next section) or any other transducer system capable of providing a volume change $\sim V_b$ and associated small pressure difference Δp between the snap-through and snap-back of a few kPa (only ~20% of the maximum pressure; Fig. 2b). This is schematically shown in Supplementary Fig. 8. Such a narrow pressure range opens up the possibility to operate a solid-state cooling system made from cheap, soft, biodegradable materials without the use of compressed air.

Voltage-controlled cycling

We demonstrate this approach by building a proof-of-concept all-soft electrical driving system using dielectric elastomer actuators (DEAs, schematic in Fig. 4a). Such a compact, cheap and all-soft plug-in-ready device directly converts electrical energy into a low-noise pneumatic actuation.

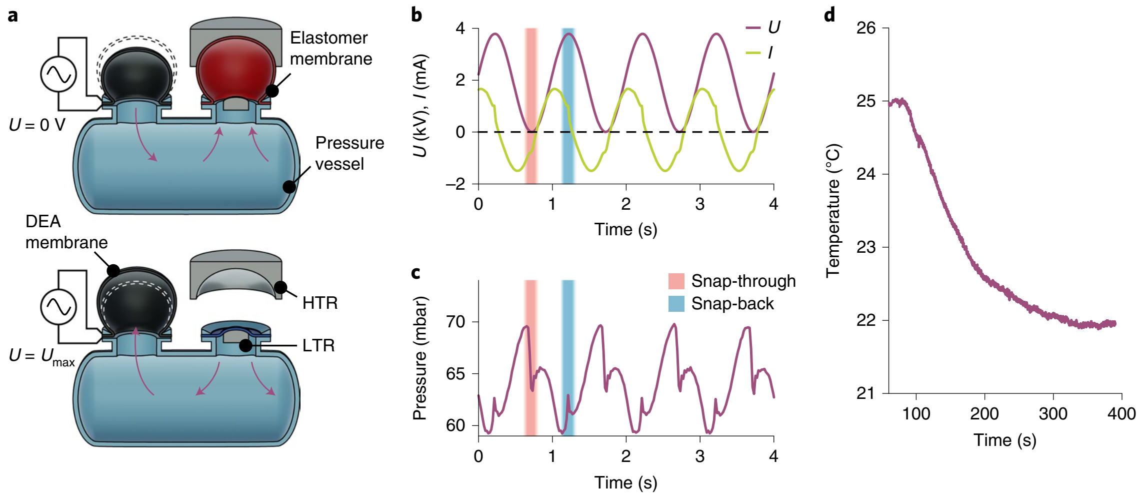

Fig. 4 | Actuated cooler design, characteristics and thermal properties. a, Schematic illustration of the DEA-actuated cooler design and functional principle. The magenta arrows indicate the exchange of gas between both balloons and the pressure vessel. The upper panel corresponds to a snap-through at low DEA voltage, and the lower panel to snap-back near the maximum applied DEA voltage, as indicated in **b**. **b**,**c**, Applied sinusoidal voltage *U*, measured current *I* and the pressure, common for both balloons, measured within the pressure vessel. Vertical coloured bars indicate the fast snap-through expansion and snap-back stages. Segments with increasing voltage (low pressure segments) correspond to a relaxed membrane on the HTR, and with large pressure to a stretched membrane on the LTR. **d**, Multi-cycle temperature evolution measured for the DEA-driven system. Temperature variations are lower than for direct pneumatic actuation due to larger LTR with a different holder layout.

A DEA is a soft capacitor, made of a deformable dielectric material, sandwiched between two compliant electrodes[49]. When a voltage is applied to the electrodes, the resulting Maxwell stress thins down the incompressible elastomer and consequently increases its area. We couple the DEA and the cooler membrane via a common sealed pressure vessel. Initial constant offset pressure inflates both the cooler membrane and the DEA at zero voltage. The overall amount of gas in the system remains constant. When voltage is applied to the DEA, its volume increases, reducing the volume of the elastomer balloon, until the snap-back is triggered. A decrease in voltage reverses this process (Fig. 4a). A high-voltage sine-wave signal allows for continuous device operation (Fig. 4b,c). The desired volume change can be adjusted by varying the voltage amplitude and the number of DEAs. The voltage-induced pressure variations (Maxwell stress) should match the snap-through and snap-back pressure difference of the NR membrane. They can be modified, changing the number of active layers in each individual (stacked) DEA (Supplementary Fig. 9). We demonstrate actuation and successful cooling (Fig. 4d, Supplementary Fig. 10 and Supplementary Video 4) with a 140 μm and a 180 μm membrane for a slightly adapted set-up geometry and frequencies of 1–3 Hz and 1–2 Hz, respectively. Remarkably, a DEA achieves even higher actuating frequencies than the design using high-pressure pulses. The COP value in this proof-of-principle demonstration is about 0.1, due to the low efficiency of electro-mechanical energy conversion. This performance metric can be further improved with more optimized transducer systems (discussion at the end of Supplementary Note 5).

Conclusion

We have demonstrated the capabilities of NR in cooling applications by constructing a prototype with outstanding cooling power ($20.9\,\mathrm{W\,g^{-1}}$, and heat flux of $256\,\mathrm{mW\,cm^{-2}}$) and good efficiency with a COP of 4.7. Controlled use of SIC results in a geCC effect, enabling devices that are stable over 10^3 inflation–deflation cycles. Further performance and stability increases are feasible with design improvements and by employing low-hysteresis and low-fatigue rubbers. Optimization of elastomer materials (that is, their SIC properties) promises to unlock the full potential of this technology. Due to the large stretches inherent in our elastomeric design, the necessary forces and pressures are small. This allows compact and lightweight set-ups for mobile applications, robotics and aircraft- and even spacecraft-related tasks. The demonstrated performance numbers put mass-market applications such as room-temperature refrigeration and air conditioning within reach of the suggested framework.

Methods

Infrared temperature measurements of NR membranes. Infrared temperature measurements were performed using a FLIR A325sc thermal camera (FLIR Systems) for real-time analysis. The camera was enclosed with a sealed housing, which allowed cooling with cold nitrogen gas to slightly below room temperature. This prevents infrared radiation from the warm camera and its reflection by the NR membrane back into the camera. The inflated membrane was shielded by Styrofoam walls, eliminating infrared reflections from various nearby thermal sources. In addition to the parasitic infrared reflections, NR is semitransparent in the infrared[50]. It is thus impossible to get consistent infrared readings from the inflated balloon (where the membrane is thin) due to the thermal contribution from the background (Fig. 3a and the initial inflation frames in Supplementary Video 3). For this reason, the temperature changes were monitored during deflation. Inflated balloons were thermalized with the surroundings (Fig. 3b) and adiabatically contracted within ~100 ms (Fig. 3c; also Fig. 2b). For reliable measurements, thick enough membranes were used (420 μm); in an unstretched state, they transmit below 7% in the infrared (thicker membranes yield similar temperatures). Membrane thickness does not affect the temperature changes for a given balloon volume V_b, as both the membrane volume V and the balloon pressure p (equation (8) in Supplementary Note 1) are proportional to it. Temperature differences were referenced to the infrared temperature of the unstretched patch of the same membrane. Supplementary Video 3 ($3.75\,\mathrm{frames\,s^{-1}}$, or $267\,\mathrm{ms\,frame^{-1}}$) evidences the abrupt temperature change upon deflation (Fig. 3b,c). This change is larger in the central area, which comes in contact with the LTR (and HTR) and depends on the balloon volume (Fig. 3e). These contact thermal reservoirs are absent in this case; thus, the membrane thermalizes much more slowly than in the regular cyclic refrigerating experiments.

Experimental realization of the geCC heat pump. For a comprehensive description and a detailed schematic of the experimental set-up, see Supplementary Fig. 1. Our geCC heat pump consists of a pressure vessel connected to two pressure reservoirs p_{high} and p_{low} via externally triggered valves (Supplementary Fig. 1a). The pressure vessel has an opening where the elastomer membrane is fixed with a clamp, so that the pressure p inside the pressure vessel is equal to the balloon pressure. The LTR was inserted from beneath (Supplementary Fig. 1b).

We measured the temperature with a type-K thermocouple fixed at the bottom of the LTR (Supplementary Fig. 1c). In order to expand the membrane, the inlet valve was opened ($p = p_{\mathrm{high}}$) while the outlet valve stayed closed. When the membrane reached its maximum volume, the inlet valve was closed and, after a specified equilibration time, the outlet valve was opened ($p = p_{\mathrm{low}}$) to initiate contraction. The experiment was controlled by a custom LabVIEW program.

p–V measurements. We measured the common pressure p inside the pressure vessel and the balloon using a Jumo dTrans p30 pressure sensor (Jumo). High-speed determination of the volume required an indirect approach. The pressure vessel was connected to an external volume of 300 l in an airtight fashion with the NR membrane facing inside (Supplementary Fig. 1a). The expansion and contraction of the membrane causes a pressure change Δp_{ext} within the external volume V_0, which we measured and converted to the change in the balloon volume ΔV_{b}, applying the ideal gas equation. The large size of the volume reservoir (300 l) in Supplementary Fig. 1 was chosen to keep the pressure increase at the low end of the sensor range. In this way, the change in the external pressure can be neglected in the key elastic equation 8 in Supplementary Note 1 and the associated equations. The sensor was connected to the reservoir via a 1,100-mm-long tube with a 3 mm diameter, in order to damp resonant oscillations of the reservoir body.

We assumed an adiabatic change of state and used the adiabatic index (heat capacity ratio) of an ideal diatomic gas, $\kappa = 1.4$.

$$\Delta V_{\mathrm{b}} = V_0 \left[1 - \left(\frac{p_0}{p_0 + \Delta p_{\mathrm{ext}}(t)} \right)^{1/\kappa} \right] \quad (4)$$

Here, p_0 is the atmosphere pressure and t is time. The mechanical input energy per cycle, W_{in}, follows from the integral work of the varying pressure during the inflation (p_{infl}) and deflation (p_{infl}) (listed in the Supplementary Note 9),

$$W_{\mathrm{in}} = \int_0^{V_{\max}} p_{\mathrm{infl}} \mathrm{d}V_{\mathrm{b}} - \int_0^{V_{\max}} p_{\mathrm{defl}} \mathrm{d}V_{\mathrm{b}} \quad (5)$$

The maximum volume ($V_{\max}$) of the inflated membrane used as upper integration limit in equation (5) was determined separately by the displacement of a water column, which yields more accurate results. The result yielded 115 cm^3 (HTR$_{\mathrm{S}}$) and 200 cm^3 (HTR$_{\mathrm{L}}$). The maximum volumes, measured with the indirect pressure conversion method using equation (4), were 5–10% lower than with the water column method. Therefore, all measured values were multiplied by a linear correction factor in order to normalize them to the accurate maximum volume.

DEA set-up and assembly. The actuator set-up is schematically illustrated in Supplementary Fig. 9a. Up to five DEAs were supported by a cuboid acrylic mount. The DEAs were fixed on the mount with clamps, as shown in Supplementary Fig. 9b,c.

Each of the DEAs driving the heat pump consisted of a layered stack of VHB 4905-F (3M) and carbon grease, shown in Supplementary Fig. 9d. One actuator layer consists of two sandwiched VHB tapes (each with a thickness of 0.5 mm; this improves dielectric breakdown strength and reliability as the defect overlap probability is low). Prior to DEA assembly, each VHB double-layer was biaxially prestretched by a factor of 1.8 (areal stretch 1.8 × 1.8). Next, the adhesive, prestretched tape was firmly pressed against the rear side of the actuator clamp. A 2-mm-wide copper tape (100 μm thick) was attached onto the membrane at the rear side of the clamp. The membrane was coated on both sides with a thin layer of carbon grease (also contacting the copper strip; Supplementary Fig. 9e, right). The copper strips were attached alternatingly on opposing sides (Supplementary Fig. 9d). All conductors of one side were connected to the same pole of the voltage source in order to subject every VHB layer to an electric field. In this work, three- and four-layer actuators were used.

For the carbon grease, Black Pearls 2000 Carbon Black (CABOT) was mixed with Elbesil 50 silicon oil (Quax) in a weight ratio of 1:15 using a planetary mixer for 10 min at 2,000 r.p.m. with five steel balls (~5 mm diameter) added and another 20 min at 2,000 r.p.m. without steel balls. Blending was interrupted in ten-minute intervals to allow cooling of the mixture for 10 min.

DEA operation. To reach a comparable degree of inflation for both the actuator and the NR membrane, the elastic response of both elements at a given common pressure p has to be similar. For comparable sizes and geometries used, the stiffness of a newly assembled DEA was found to be slightly higher than that of the NR balloon. We used two methods to adjust the DEA elasticity to better match the membrane response. One method is to let the DEA rest for several hours, allowing the silicon oil of the carbon grease electrodes to diffuse into the VHB layers, acting as a softener. The other is to initially inflate the DEA to volumes larger than the typical operating volumes a few times, causing softening of the membranes due to the Mullins effect. We applied an offset pressure of 5,500–7,500 Pa for operation and electrically actuated the DEA system with a high-voltage sine-wave signal (Trek 610D high-voltage amplifier) at an amplitude of up to 3,700 V and frequencies between 1 and 3 Hz (Supplementary Video 4).

Data availability

The datasets generated and/or analysed during the current study are available within the paper and its Supplementary Information. Other materials are available from the corresponding author, M.K., upon reasonable request.

Received: 1 July 2020; Accepted: 18 December 2020;
Published online: 28 January 2021

References

1. *The Future of Cooling* (OECD/IEA, 2018).
2. Goetzler, W., Zogg, R., Young, J. & Johnson, C. Alternatives to vapor-compression HVAC technology. *ASHRAE J.* **56**, 12–23 (2014).
3. Wang, R. et al. Torsional refrigeration by twisted, coiled, and supercoiled fibers. *Science* **366**, 216–221 (2019).
4. Wang, Y. et al. A high-performance solid-state electrocaloric cooling system. *Science* **370**, 129–133 (2020).
5. Kasaeian, A. et al. Applications of eco-friendly refrigerants and nanorefrigerants: a review. *Renew. Sustain. Energy Rev.* **96**, 91–99 (2018).
6. Xie, Z. J., Sebald, G. & Guyomar, D. Comparison of elastocaloric effect of natural rubber with other caloric effects on different-scale cooling application cases. *Appl. Therm. Eng.* **111**, 914–926 (2017).
7. Mañosa, L. & Planes, A. Solid-state cooling by stress: a perspective. *Appl. Phys. Lett.* **116**, 050501 (2020).
8. Imran, M. & Zhang, X. Recent developments on the cyclic stability in elastocaloric materials. *Mater. Des.* **195**, 109030 (2020).
9. Greco, A., Aprea, C., Maiorino, A. & Masselli, C. A review of the state of the art of solid-state caloric cooling processes at room-temperature before 2019. *Int. J. Refrig.* **106**, 66–88 (2019).
10. Kitanovski, A., Plaznik, U., Tomc, U. & Poredoš, A. Present and future caloric refrigeration and heat-pump technologies. *Int. J. Refrig.* **57**, 288–298 (2015).
11. Goetzler, W., Zogg, R., Young, J. & Johnson, C. *Energy Savings Potential and RD&D Opportunities for Non-vapor-Compression HVAC Technologies* 199 (Navigant Consulting Inc., prepared for US Department of Energy, 2014).
12. Ma, R. et al. Highly efficient electrocaloric cooling with electrostatic actuation. *Science* **357**, 1130–1134 (2017).
13. Li, B. et al. Colossal barocaloric effects in plastic crystals. *Nature* **567**, 506–510 (2019).
14. Carvalho, A. M. G., Imamura, W., Usuda, E. O. & Bom, N. M. Giant room-temperature barocaloric effects in PDMS rubber at low pressures. *Eur. Polym. J.* **99**, 212–221 (2018).
15. Tušek, J., Engelbrecht, K., Mikkelsen, L. P. & Pryds, N. Elastocaloric effect of Ni-Ti wire for application in a cooling device. *J. Appl. Phys.* **117**, 124901 (2015).
16. Pieczyska, E., Gadaj, S., Nowacki, W. & Tobushi, H. Phase-transformation fronts evolution for stress- and strain-controlled tension tests in TiNi shape memory alloy. *Exp. Mech.* **46**, 531–542 (2006).
17. Frenzel, J., Eggeler, G., Quandt, E., Seelecke, S. & Kohl, M. High-performance elastocaloric materials for the engineering of bulk- and micro-cooling devices. *MRS Bull.* **43**, 280–284 (2018).
18. Porenta, L. et al. Thin-walled Ni-Ti tubes under compression: ideal candidates for efficient and fatigue-resistant elastocaloric cooling. *Appl. Mater. Today* **20**, 100712 (2020).
19. Bruederlin, F. et al. Elastocaloric cooling on the miniature scale: a review on materials and device engineering. *Energy Technol.* **6**, 1588–1604 (2018).
20. Engelbrecht, K. Future prospects for elastocaloric devices. *J. Phys. Energy* **1**, 021001 (2019).
21. Cong, D. et al. Colossal elastocaloric effect in ferroelastic Ni-Mn-Ti Alloys. *Phys. Rev. Lett.* **122**, 255703 (2019).
22. Kirsch, S.-M. et al. NiTi-based elastocaloric cooling on the macroscale: from basic concepts to realization. *Energy Technol.* **6**, 1567–1587 (2018).
23. le Cam, J. B. Energy storage due to strain-induced crystallization in natural rubber: the physical origin of the mechanical hysteresis. *Polymer* **127**, 166–173 (2017).
24. Wiegand, W. & Snyder, J. The rubber pendulum, the Joule effect, and the dynamic stress-strain curve. *Rubber Chem. Technol.* **8**, 151–173 (1935).
25. Strong, C. L.The amateur scientist: some delightful engines driven by the heating of rubber bands. *Sci. Am.* **224**, 118–122 (1971).
26. Lyon, R. E., Wang, D., Farris, R. & MacKnight, W. Polyurethane–urea elastomers as working substances in rubber heat engines. *J. Appl. Polym. Sci.* **29**, 2857–2872 (1984).
27. Mullen, J., Look, G. W. & Konkel, J. Thermodynamics of a simple rubber-band heat engine. *Am. J. Phys.* **43**, 349–353 (1975).
28. Farris, R. J. Rubber heat engines, analyses and theory. *Polym. Eng. Sci.* **17**, 737–744 (1977).
29. Hutchinson, W. D. *Manually Operated Elastomer Heat Pump* Report no. NPO-10677, 2 (NASA, 1970).
30. Gerlach, D. W. in *ASME 2009 International Mechanical Engineering Congress and Exposition* 289–293 (American Society of Mechanical Engineers, 2009).

31. Sebald, G., Komiya, A., Jay, J., Coativy, G. & Lebrun, L. Regenerative cooling using elastocaloric rubber: analytical model and experiments. *J. Appl. Phys.* https://doi.org/10.1063/1.5132361 (2020).
32. Huneau, B. Strain-induced crystallization of natural rubber: a review of X-ray diffraction investigations. *Rubber Chem. Technol.* **84**, 425–452 (2011).
33. le Cam, J. B. Strain-induced crystallization in rubber: a new measurement technique. *Strain* **54**, e12256 (2018).
34. Keplinger, C., Li, T. F., Baumgartner, R., Suo, Z. G. & Bauer, S. Harnessing snap-through instability in soft dielectrics to achieve giant voltage-triggered deformation. *Soft Matter* **8**, 285–288 (2012).
35. Baumgartner, R. et al. A lesson from plants: high-speed soft robotic actuators. *Adv. Sci.* **7**, 1903391 (2020).
36. Jacobs, S. et al. The performance of a large-scale rotary magnetic refrigerator. *Int. J. Refrig.* **37**, 84–91 (2014).
37. Clot, P. et al. A magnet-based device for active magnetic regenerative refrigeration. *IEEE Trans. Magn.* **39**, 3349–3351 (2003).
38. Tura, A. & Rowe, A. Permanent magnet magnetic refrigerator design and experimental characterization. *Int. J. Refrig.* **34**, 628–639 (2011).
39. Defay, E. et al. Enhanced electrocaloric efficiency via energy recovery. *Nat. Commun.* **9**, 1827 (2018).
40. Bruederlin, F., Ossmer, H., Wendler, F., Miyazaki, S. & Kohl, M. SMA foil-based elastocaloric cooling: from material behavior to device engineering. *J. Phys. D Appl. Phys.* **50**, 424003 (2017).
41. Tušek, J. et al. A regenerative elastocaloric heat pump. *Nat. Energy* **1**, 16134 (2016).
42. Ossmer, H. et al. Energy-efficient miniature-scale heat pumping based on shape memory alloys. *Smart Mater. Struct.* **25**, 085037 (2016).
43. Merritt, D. R. & Weinhaus, F. The pressure curve for a rubber balloon. *Am. J. Phys.* **46**, 976–977 (1978).
44. Gent, A. N. A new constitutive relation for rubber. *Rubber Chem. Technol.* **69**, 59–61 (1996).
45. Khiêm, V. N. & Itskov, M. Analytical network-averaging of the tube model: strain-induced crystallization in natural rubber. *J. Mech. Phys. Solids* **116**, 350–369 (2018).
46. Gros, A., Verron, E. & Huneau, B. A physically-based model for strain-induced crystallization in natural rubber. Part II: derivation of the mechanical model. *J. Mech. Phys. Solids* **125**, 255–275 (2019).
47. Plagge, J. & Kluppel, M. A theory relating crystal size, mechanical response, and degree of crystallization in strained natural rubber. *Macromolecules* **51**, 3711–3721 (2018).
48. Moran, M. J., Shapiro, H. N., Boettner, D. D. & Bailey, M. B. *Fundamentals of Engineering Thermodynamics* 9th edn (Wiley, 2018).
49. Suo, Z. G. Theory of dielectric elastomers. *Acta Mech. Solid. Sin.* **23**, 549–578 (2010).
50. Williams, D. & Dale, B. Further studies of the infrared absorption of rubber. *Rubber Chem. Technol.* **18**, 10–19 (1945).

Acknowledgements

We dedicate this work to S. Bauer. This work was supported by the ERC Starting Grant 'GEL-SYS' under grant agreement no. 757931 and start-up funding of the Linz Institute of Technology 'Soft Electronics Laboratory' under grant no. LIT013144001SEL.

Author contributions

F.G. and R.S. designed and fabricated the geCC heat pump and the DEA-triggered cooler and performed all experiments and measurements associated with these devices. R.B., A.K. and R.S. performed the infrared measurements. F.G., M.D. and G.M. performed the tensile tests. G.M. conducted the simulation; N.A. developed the theoretical framework.; and F.G., R.S. and N.A. analysed data. F.G., D.W., M.D. and G.M. prepared figures, and D.W., F.G. and G.M. prepared videos with contributions from all authors. F.G., N.A., R.S. and M.K. wrote the manuscript with comments from all authors. G.M., D.W., R.S. and J.S. contributed to editing the manuscript. S.B., R.S., N.A. and M.K. supervised the project.

Competing interests

The authors declare no competing interests.

Additional information

Supplementary information is available for this paper at https://doi.org/10.1038/s41560-020-00770-w.

Correspondence and requests for materials should be addressed to M.K.

Peer review information *Nature Energy* thanks Manfred Kohl and the other, anonymous, reviewer(s) for their contribution to the peer review of this work.

Reprints and permissions information is available at www.nature.com/reprints.

Publisher's note Springer Nature remains neutral with regard to jurisdictional claims in published maps and institutional affiliations.

Supplementary Materials for

Elastocaloric heat pump with specific cooling power of 20.9 W/g, exploiting snap-through instability and strain-induced crystallization

Florian Greibich, Reinhard Schwödiauer, Guoyong Mao, Daniela Wirthl, Michael Drack, Richard Baumgartner, Alexander Kogler, Josef Stadlbauer, Siegfried Bauer, Nikita Arnold and Martin Kaltenbrunner*.

Correspondence to: martin.kaltenbrunner@jku.at

This PDF file includes:

Supplementary Notes 1-9
Supplementary Figures 1 to 10
Supplementary Table 1

Other Supplementary Materials for this manuscript include the following:

Supplementary Videos V1 to V4

Supplementary Notes

Supplementary Note 1. Thermodynamic framework

Refrigerating action of the suggested setup is based on the *adiabatic* heating of the natural rubber (NR) upon its fast stretching. Increase in temperature is understandable, as the stretching force (inflating overpressure in our design) performs positive work on the NR. However, the *magnitude* of this change is unexpectedly large and exceeds the values predicted by the simple elastocaloric consequences of conventional rubber elasticity.

Disproportionate temperature increase *at large stretches* is due to strain-induced crystallization (SIC), which is an exothermal 1st order phase transition[1]. New insights emerge from resent experimental data on SIC, utilizing modern XRD and synchrotron radiation analysis of NR and similar materials[2-12]. Caloric effects of SIC were investigated mainly in uniaxial stretching geometries[7,10,13-19] and at stretch rates that make deviations from adiabaticity unavoidable and essential[18,20,21]. Theories of SIC are numerous, at times contradictory, and are often ambiguous for small stretches and/or non-uniaxial geometries[2,7,13,22-33]. In this work, we stay within the general thermodynamic framework, which provides a fitting explanation of our experimental findings, and emphasized difference to a *conventional* elastocaloric effects in elastomers. In the presence of SIC, the Helmholtz free energy density of an incompressible elastomer with constant thermophysical parameters and varying crystalline fraction χ can be written as[2,29]:

$$F = cT - \chi U_{\mathrm{ac}} - T\left(-\chi \frac{U_{\mathrm{ac}}}{T_{\mathrm{c},0}} + S_{\mathrm{ch}}[\lambda,\chi] + c\ln\frac{T}{T_S}\right) \tag{1}$$

Here c is the heat capacity per unit (constant) *volume*. The first two terms describe the internal energy U; the term $-\chi U_{\mathrm{ac}}$ reflects *lower energy* of the crystalline state, where $U_{\mathrm{ac}} = \rho\Delta H > 0$ is the latent heat (per unit volume) of crystallization (density ρ and the value per mass ΔH are listed in Supplementary Note 9). The expression in the brackets is the *non-equilibrium total* entropy S. The first two terms in brackets are configurational, while the third term is thermal, $S_{\mathrm{thermal}} = c\ln(T/T_S)$. The term $-\chi S_{\mathrm{ac}} = -\chi U_{\mathrm{ac}}/T_{\mathrm{c},0}$ accounts for change in *configurational* entropy of the individual *structural units*, which is lower by S_{ac} in the crystalline state. The terms with U_{ac} and S_{ac} compete in free energy $F = U - TS$, making unstretched crystallization favourable for $T < T_{\mathrm{c},0}$; this yields the relation $S_{\mathrm{ac}} = U_{\mathrm{ac}}/T_{\mathrm{c},0}$ used in eq. (1).

The term $S_{\mathrm{ch}}[\lambda,\chi]$ describes *configurational* entropy of the partially crystallized, stretched *chains*[22]. We assume spatial homogeneity and reduction to one principal stretch, using incompressibility and geometry (uniaxial, equal-biaxial, etc.).

With T,λ being constant, the system adjusts its crystallinity to minimize free energy. Equilibrium crystallinity χ_{eq} follows from zero of derivative of eq. (1) with respect to χ:

$$U_{\mathrm{ac}}\left(\frac{1}{T_{\mathrm{c},0}}-\frac{1}{T}\right)=S_{\mathrm{ch},\chi}[\lambda,\chi_{\mathrm{eq}}] \tag{2}$$

Equation (2) defines an implicit function $\chi_{\mathrm{eq}}(T,\lambda)$. By substituting it into eq. (1) we obtain the equilibrium free energy $F(T,\lambda,\chi_{\mathrm{eq}}(T,\lambda))=F_{\mathrm{eq}}(T,\lambda)$, which depends on the native variables T,λ only. Equilibrium entropy and internal energy (in these variables) are obtained in the same way. Entropy separation into configurational and thermal parts becomes physical, rather than mathematical, because the (equilibrium) $S_{\mathrm{config}}(\lambda,T)=-\chi_{\mathrm{eq}}(\lambda,T)\frac{U_{\mathrm{ac}}}{T_{\mathrm{c},0}}+S_{\mathrm{ch}}[\lambda,\chi_{\mathrm{eq}}(\lambda,T)]$ now depends on T as well. Considering the full differential of the entropy from eq. (1), we obtain for the adiabat $dS=0$.

$$c\frac{dT}{T}\overset{1}{=}\left(\frac{U_{\mathrm{ac}}}{T_{\mathrm{c},0}}-S_{\mathrm{ch},\chi}[\lambda,\chi]\right)d\chi-S_{\mathrm{ch},\lambda}[\lambda,\chi]d\lambda\overset{2}{=}\frac{U_{\mathrm{ac}}}{T}d\chi-S_{\mathrm{ch},\lambda}[\lambda,\chi]d\lambda \tag{3}$$

Expression $(3)_1$ is general, while in eq. $(3)_2$ we substituted $S_{\mathrm{ch},\chi}$ from the equilibrium crystallization condition (2). The final expression generalizes adiabatic heating of the fully amorphous elastomer upon stretch – the last term in eq. $(3)_2$, where chain entropy decreases with λ. As χ_{eq} increases with λ, the latent heat $U_{ac}>0$ leads to an additional heating.

Let us analyse the behaviour of different terms in eq. (1) for $\lambda=const$, where changes are only due to crystallinity χ. Both sides of eq. (2) are positive above the unstretched crystallization temperature $T>T_{\mathrm{c},0}$. Thus, equilibrium *chain* entropy S_{ch} increases with crystallinity, and therefore *decreases with T*, on the iso-stretch curves. The partial derivative of the *total configurational* entropy is:

$$S_{\mathrm{config},\chi}(\lambda,\chi)=-\frac{U_{\mathrm{ac}}}{T_{\mathrm{c},0}}+S_{\mathrm{ch},\chi}[\lambda,\chi]\overset{\mathrm{eq}}{=}-\frac{U_{\mathrm{ac}}}{T}<0 \tag{4}$$

The last equality utilized equilibrium condition (2). Thus, for $\lambda=const$, *total configurational* entropy S_{config} decreases with χ, and *increases* with *T*.

The last term in eq. (3)$_2$ is related to the (nominal) stress, which we now calculate, starting from eq. (1), using $F_{\mathrm{eq}}(T,\lambda)=F(T,\lambda,\chi_{\mathrm{eq}}(T,\lambda))$ and chain rule. We write uniaxial expression, equal-biaxial stress is half of this value, but it should be counted two times, so that the energetic relation $\tfrac{1}{2}s\times 2d\lambda = sd\lambda = dF_{\mathrm{eq}}$ and the definition of *s* as derivative of *F* remain valid.

$$\begin{aligned}
&s\overset{1}{=}F_{\mathrm{eq},\lambda}(T,\lambda)\overset{2}{=}\\
&\chi_{\mathrm{eq},\lambda}(T,\lambda)U_{\mathrm{ac}}\left(\frac{T}{T_{\mathrm{c},0}}-1\right)-T\left(S_{\mathrm{ch},\lambda}[\lambda,\chi_{\mathrm{eq}}(T,\lambda)]+S_{\mathrm{ch},\chi}[\lambda,\chi_{\mathrm{eq}}(T,\lambda)]\chi_{\mathrm{eq},\lambda}(T,\lambda)\right)\overset{3}{=}\\
&\left(U_{\mathrm{ac}}\left(\frac{T}{T_{\mathrm{c},0}}-1\right)-TS_{\mathrm{ch},\chi}[\lambda,\chi_{\mathrm{eq}}(T,\lambda)]\right)\chi_{\mathrm{eq},\lambda}(T,\lambda)-TS_{\mathrm{ch},\lambda}[\lambda,\chi_{\mathrm{eq}}(T,\lambda)]\overset{4}{=}\\
&-TS_{\mathrm{ch},\lambda}[\lambda,\chi_{\mathrm{eq}}(T,\lambda)]
\end{aligned}\tag{5}$$

Equation (5)$_1$ is the definition; eq. (5)$_2$ is differentiation using chain rule; eq. (5)$_3$ regroups the terms, so that the expression in the outermost parenthesis disappears due to the equilibrium condition (2); eq. (5)$_4$ is the final result. It *differs* from the purely *chain-entropic* expression, which would contain $S_{\mathrm{eq},\lambda}[T,\lambda]=S_{\mathrm{ch},\lambda}[\lambda,\chi_{\mathrm{eq}}(T,\lambda)]+S_{\mathrm{ch},\chi}[\lambda,\chi_{\mathrm{eq}}(T,\lambda)]\chi_{\mathrm{eq},\lambda}(T,\lambda)$. In the transition from eq. (5)$_{2,3}$ to eq. (5)$_4$, the second *part* of the *total* entropic contribution (which also includes the change in configurational entropy of the structural units, $-\chi U_{\mathrm{ac}}/T_{\mathrm{c},0}=-\chi S_{\mathrm{ac}}$) cancels with the *energetic* contribution to the stress, $s_U=-U_{\mathrm{ac}}\chi_{\mathrm{eq},\lambda}(T,\lambda)$.

This explains the meaning of the *adiabatic* relation (3)$_2$. Multiplying everything by *T* and replacing $-TS_{\mathrm{ch},\lambda}[\lambda,\chi]$ by the equilibrium stress *s* from (5)$_4$, we obtain:

$$cdT=U_{\mathrm{ac}}d\chi+s[T,\lambda,\chi_{\mathrm{eq}}(T,\lambda)]d\lambda \tag{6}$$

Equation (6) relates the differentials along the *equilibrium adiabat*, using *equilibrium* stress and, together with the equilibrium condition (2), describes the temperature change upon deformation. For detailed description, the function $S_{\mathrm{ch}}[\lambda,\chi]$ has to be derived in a microscopic theory. However, it is known from the experiments, that stress $s\geq 0$ and that the crystallinity χ increases with stretch λ. Therefore both heating terms on the r.h.s. in eq. (6) remain positive with increasing λ. Because the internal energy density $U=cT-\chi U_{\mathrm{ac}}$, eq. (6) presents *adiabatic* energy balance $dU=sd\lambda$, which holds even *with irreversible processes* present, where $TdS>\delta Q=0$. However, this simplicity contains subtleties, related to the temperature and phase changes.

Without the SIC, elastomeric stress is due to configurational entropy only, and eq. (6) simplifies to:

$$cdT = -TS_{\mathrm{ch},\lambda}[\lambda]d\lambda = -TdS_{\mathrm{ch}}[\lambda] \tag{7}$$

This reflects differential conservation of total configurational and thermal entropy in eq. (1), $S_{\mathrm{ch}}[\lambda] + c\ln T / T_S = const$. In its full form, eq. (6) permits estimation of the SIC contribution from the *experimental* data, without resorting to a particular microscopic model. Indeed, the last $sd\lambda$ term represents the work of external forces, provided by the inflating overpressure in balloon experiments. For the spherical case in our notations it can be expressed in the general form of eq. (S2)1 from ref.[34]:

$$p = \frac{H}{R}\frac{F_{\mathrm{eq},\lambda}(T,\lambda)}{\lambda^2} \tag{8}$$

Here, H and R are the *initial* thickness and radius of the (equivalent) thin spherical membrane with the constant material volume $V = 4\pi R^2 H$, and λ the *lateral* stretch. The membrane volume was calculated for an initially flat circular patch with radius r and thickness H as $V = \pi r^2 H \approx 4\pi R^2 H$, so that $R \approx r/2$. The differential of the *balloon* volume is $dV_{\mathrm{b}} = 4\pi R^3 \lambda^2 d\lambda$, and the differential work is:

$$pdV_{\mathrm{b}} = 4\pi R^2 H F_{\mathrm{eq},\lambda}(T,\lambda)d\lambda = Vs[T,\lambda]d\lambda \tag{9}$$

This allows to replace the last (stress) term in eq. (6) by the work done by the gas during the balloon inflation/deflation. Stress change due to *adiabatic* temperature increase during the inflation is automatically accounted for in the *experimental* adiabatic pressure-volume curve. This leads to the following estimation, for the *average* temperature and crystallinity for the whole membrane (see Supplementary Fig. 5 for the distribution of stretch across the balloon):

$$c\Delta T_{\mathrm{av}} = U_{\mathrm{ac}}\chi + V^{-1}\int pdV_{\mathrm{b}} \tag{10}$$

This holds even for irreversible adiabatic processes, where $TdS > \delta Q = 0$. We apply eq. (10) to analyse *deflation*, where reliable IR (infrared) temperature measurements can be performed. The measured pressure deflation integrals are $\int p_{\mathrm{defl}} dV_{\mathrm{b}} = 0.71$ and 1.1 J for HTRS and HTRL, respectively (Supplementary Note 9). *Without* the SIC term, eq. (10) predicts $\Delta T_{\mathrm{av}} = 4.2$ and 6.5 K for both cases. The values *measured* with the IR camera are noticeably larger: $\Delta T_{\mathrm{av}} = 8.9$ and 12.1 K (Fig. 3e). This shows, that the SIC contribution to the adiabatic temperature change is essential: 53 % and 46 %, respectively. *Average* crystallinity, calculated from the eq. (10) using *measured* integrals and temperatures is $\chi = 0.23$ and 0.27 for HTRS and $\mathrm{HTR_L}$, respectively. These values comply with the XRD results for large uniaxial stretches[4,18].

Measured values for the *central* part of the membrane *in contact with the LTR* are even higher: ΔT_{mem} = 11.1 and 14.1 K (Fig. 3e, they are used in section "Simulation of the heat pump characteristics" below). The *maximum* temperature change in the very centre reaches 13.1 and 15.3 K upon deflation. The full inflation-deflation temperature change of the membrane exceeds 23 K.

Supplementary Note 2. Hysteresis in Stress-Strain and Pressure-Volume measurements

Experimental *p*-*V* diagrams for the balloon actuation cycle (similar to Fig. 2b) demonstrate significant hysteresis, of the order of 10-22 % of the area under the inflation curve, which enters the COP calculations below. Several interrelated factors contribute to this hysteresis.

i) Purely thermal, conventional elastocaloric effects. For Carnot process, they define the minimum possible hysteresis and net mechanical input energy. Our setup is closer to an Otto cycle. In an ideal elastomer without SIC, the inflation adiabat is hotter than the deflation adiabat due to heat exchange of the membrane with the reservoirs. The stress and overpressure in eq. (8) are proportional to the shear modulus μ, which for elastomers is proportional to T. Thus, such a hysteresis would be *smaller* than the maximum relative changes in (absolute) temperature, predicted by the *conventional elastocaloric effect*, i.e., $\Delta\mu/\mu \sim \Delta T/T \sim 1.6-2.9\%$, which is several times smaller than the experimental values.

ii) SIC contribution to the temperature and stress. As SIC exothermally enhances the temperature changes (in both directions), the temperature difference between the inflation and deflation adiabats increases. SIC also strongly modifies the stress-stretch curves. Assuming that these alterations are comparable for both adiabats, we estimate the expected hysteresis as in i), using *measured* IR ΔT values, which reflect SIC heating contribution: $\Delta T/T \sim 3-4.1\%$. This is still much lower than the observed hysteresis values.

iii) Non-equilibrium SIC kinetics. SIC is by far the dominant factor in hysteresis according to refs.[3,7,18,29,30,32]. The assessment of SIC contribution differs in the literature, due to complexity of its behaviour, see refs.[3,28,29].

SIC is reversible, as the system always returns to the same initial non-crystallized state, and (after a few initial cycles) goes through *the same* (partially crystallized) stages in repeated cycling. However, this cycling is *not thermodynamically* reversible, or equilibrium, because the crystallization on the inflation leg requires an overstretching, while amorphization on the deflation/contraction leg does not. As a result, crystallinity is higher for contraction at the same λ, (Fig. 2c), and such a cycle cannot be run in a reversed direction. The hysteresis is non-dissipative[20], i.e., eq. (10) contains no other frictional or viscoelastic terms during *fast, adiabatic* expansion/contraction. The energy enclosed by the hysteresis loop is ultimately transferred to the surrounding. In balloon cycling experiments this happens on the HTR and LTR reservoirs, while fast inflation/deflation stages (<100 ms) remain quasi-adiabatic. In *much slower* cyclic uniaxial tensile tests (>3 s) heat exchange happens during the whole cycle. After several cycles, the hysteresis work is balanced by the heat losses to the ambient.

To understand the elastic properties and hysteretic behaviour of NR[19] we characterized our membranes with *uniaxial* tensile tests. Measurements were performed up to a maximum stretch of 7.5 and 2.7 (Supplementary Fig. 2) to investigate the behaviour with and without SIC respectively. The value of hysteresis (defined as the area within the hysteretic curve) was plotted for each cycle. Initial values decrease due to the Mullins effect[35], and stabilize near some constant value after several (5-10) cycles. There was *no* delay between the cycles, or stretching and contraction; with 30 s holding time between these stages the hysteresis was 10-25 % larger. Noticeable hysteresis exists only for large stretches. Low stretch rates at the top are nearly isothermal, while higher stretch cycles at the bottom have periods of 6 s. In an ideal (even irreversible) uniaxial adiabatic experiments eq. (10) reads: $c\Delta T = U_{\mathrm{ac}}\chi + \int s d\lambda$. This implies higher temperature at the contraction leg, because the crystallinity χ is *known* to be higher there and $\oint s d\lambda > 0$ between the states with the same λ. The hysteresis loop is similar for slow and fast stretching; therefore, it is dominated by the (kinetic) differences in the $U_{\mathrm{ac}}\chi$ term, rather than differences in temperature [18]. Hysteretic work heats the elastomer, which (in stationary cycling) is balanced by the heat losses to the (colder) surrounding. There is no noticeable difference between the slow and fast cycling in Supplementary Fig. 2. This suggests, that adiabatic conditions are unfeasible in such uniaxial experiments, because they cannot be performed fast enough. In contrast, our balloon setup contains *more than 30 times* faster inflation/deflation snap-through legs, where quasi-adiabatic conditions are reached.

iv) Viscoelasticity and frictional dissipation with heating. Viscoelastic effects are by definition low in an ideal elastic material[36,37]. Various theories of viscoelastic behaviour of elastomers can be found in refs.[37-41], and in application to hysteresis in inflatable elastomeric balloons in refs.[42,43]. However, NR is virtually *non-viscoelastic* (see e.g., comparison with VHB in Fig. 2a from ref.[34]), and other frictional losses are also negligible in our setup.

Supplementary Note 3. Simulation of the heat pump characteristics

Parasitic heat exchange with the surrounding is difficult to quantify, which precludes the determination of heat pump characteristics at the later stages of a multicycle cooling curve. We estimate the performance of a perfectly isolated system by analysing the corresponding temperature curve over the course of the entire cooling process. Starting point is the *maximum* possible adiabatic NR *membrane* temperature change $\Delta T_{\mathrm{mem}} = T_0 - T_{\mathrm{mem}}$ (and the associated absolute value T_{mem}). They are determined from the IR-measurements (see Methods section "Infrared temperature measurements of NR membranes", Fig. 3e, and Supplementary Note 9). The influence of the parasitic heat exchange was deduced comparing this value with the *measured* stationary LTR temperature span in cycling experiments, $\Delta T_{\mathrm{meas}} = T_0 - T_{\mathrm{meas}}$ (and/or the absolute value T_{meas}, also listed in Supplementary Note 9). The signs and notations here and below are chosen such, that the relevant quantities are positive.

In cycling experiments, the LTR temperature T evolves due to repeated cooling by the membrane and the parasitic heating from the background:

$$\dot{T} = \alpha(T_{\mathrm{mem}} - T) + \gamma(T_0 - T) \tag{11}$$

In this section, unless explicitly stated otherwise, T refers to the slow evolution of the LTR temperature in cycling experiments. In the previous "Thermodynamic framework" section, T denoted the temperature of the NR membrane in a fast, single inflation/deflation process. The 1st term describes cooling from the starting (background) temperature T_0 to the minimum theoretically possible value $T_{\mathrm{mem}} = T_0 - \Delta T_{\mathrm{mem}}$ in the absence of parasitic heat, which proceeds with rate constant α. The 2nd term describes parasitic heating by the background, which intensifies with cooling, characterized by rate constant γ. These constants are related to the LTR heat exchange with the membrane and surrounding respectively. They cannot be measured directly, but their order of magnitude is given by the eqs. (26)-(27). Because $T_{\mathrm{mem}} < T < T_0$, the 1st term is negative (cooling) and the 2nd positive (heating). The solution of the differential eq. (11) is:

$$T = T_{\mathrm{meas}} + \Delta T_{\mathrm{meas}} e^{-\lambda t}, \qquad \dot{T} = -\lambda \Delta T_{\mathrm{meas}} e^{-\lambda t} \tag{12}$$

Mathematically, the constants $T_{\mathrm{meas}}, \Delta T_{\mathrm{meas}}, \lambda$ are related to the parameters $T_{\mathrm{mem}}, \Delta T_{\mathrm{mem}}, \alpha, \gamma$ defined above via the initial and stationary conditions and the overall temperature modification rate:

$$\Delta T_{\text{meas}} = \frac{\alpha}{\gamma + \alpha}\Delta T_{\text{mem}}, \quad T_{\text{meas}} = T_0 - \Delta T_{\text{meas}}, \qquad \lambda = \alpha + \gamma \tag{13}$$

Experimentally, T_{meas} is the temperature for $t \to \infty$; ΔT_{meas} is its absolute deviation from the background temperature; $T_{\text{meas}}, \Delta T_{\text{meas}}, \lambda$ can be found from the exponential fitting of the measured cooling curves. This allows to find the rate constants α and γ from relations (13):

$$\alpha = \lambda\frac{\Delta T_{\text{meas}}}{\Delta T_{\text{mem}}}, \quad \gamma = \lambda\left(1 - \frac{\Delta T_{\text{meas}}}{\Delta T_{\text{mem}}}\right) \tag{14}$$

It is convenient to introduce the positive deviation of LTR temperature from the background value:

$$\Delta T \overset{\text{def}}{=} T_0 - T = \Delta T_{\text{meas}}(1 - e^{-\lambda t}) > 0 \tag{15}$$

This temperature difference is used in the axes of Figs. 2e-f and Supplementary Figs. 4b-f. With these notations we can determine the contribution of all terms in eq. (11). In terms of associated energy flow, they can be written as:

$$-q_{\text{effective}} = -q_{\text{intrinsic}} + q_{\text{parasitic}}, \quad \text{or} \qquad q_{\text{intrinsic}} = q_{\text{effective}} + q_{\text{parasitic}} \tag{16}$$

The signs are chosen to make all heat fluxes positive. For the sake of generality, we consider fluxes per area, which are related to LTR temperature deviations via a common constant $c = \frac{c_{\text{LTR}} m_{\text{LTR}}}{A_{\text{LTR}}}$, which depends on setup geometry. Here, c_{LTR}, m_{LTR} and A_{LTR} are the specific heat capacity, mass and area of the LTR, listed in the Supplementary Note 9. The fluxes in eq. (16) become:

$$\begin{aligned}
q_{\text{effective}} &= -c\dot{T} &&= c\lambda\Delta T_{\text{meas}} e^{-\lambda t} &&= c\lambda(\Delta T_{\text{meas}} - \Delta T) \\
q_{\text{intrinsic}} &= -c\alpha(T_{\text{mem}} - T) &&= c\alpha(T_{\text{meas}} - T_{\text{mem}} + \Delta T_{\text{meas}} e^{-\lambda t}) &&= c\alpha(\Delta T_{\text{mem}} - \Delta T) \\
q_{\text{parasitic}} &= c\gamma(T_0 - T) &&= c\gamma\Delta T_{\text{meas}}(1 - e^{-\lambda t}) &&= c\gamma\Delta T
\end{aligned} \tag{17}$$

The 1st equalities substitute the definitions (11) multiplied by c, the 2nd ones use eq. (12), and the 3rd ones express the result via the variable, time-dependent temperature difference from eq. (15). Finally, we consider the ideal lossless system without the parasitic term, i.e., $\gamma = 0$ in eqs. (11)-(17). This yields the ideal temperature behaviour and heat flux:

$$T_{\text{ideal}} = T_{\text{mem}} + \Delta T_{\text{mem}} e^{-\alpha t}, \qquad \Delta T_{\text{ideal}} \overset{\text{def}}{=} T_0 - T_{\text{ideal}} = \Delta T_{\text{mem}}(1 - e^{-\alpha t}) \tag{18}$$

$$q_{\text{ideal}} = -c\dot{T}_{\text{ideal}} = c\alpha\Delta T_{\text{mem}} e^{-\alpha t} = c\alpha(\Delta T_{\text{mem}} - \Delta T_{\text{ideal}}) \tag{19}$$

Fluxes from the eqs. (17), (19) are depicted in Supplementary Fig. 4 as functions of time (a), and as functions of their respective ΔT (b). All fluxes can be recalculated into the total cooling power using LTR area from the Supplementary Note 9. The maximal value in Supplementary Figs. 4a-b corresponds to a total cooling power of 877 mW. Note, that in its region of definition, the indirectly *measured* intrinsic value coincides with the ideal, $q_{\text{intrinsic}}(\Delta T) = q_{\text{ideal}}(\Delta T_{\text{ideal}})$, which cannot be measured. The *heat power* transported from the LTR via *any* of the channels (17) is given by the corresponding flux multiplied by the LTR area:

$$\dot{Q} = qA_{\text{LTR}} \tag{20}$$

The mechanical *input power* $\dot{W}_{\text{in}}$ is given by the input energy per cycle W_{in} from eq. (5) in main text, divided by the cycle period t_{cycle}:

$$\dot{W}_{\text{in}} = W_{\text{in}} / t_{\text{cycle}} \tag{21}$$

The COP and the SCP for each channel are defined by

$$\text{COP} = \frac{Q}{W_{\text{in}}} = \frac{\dot{Q}}{\dot{W}_{\text{in}}} = \frac{qA_{\text{LTR}}}{\dot{W}_{\text{in}}}, \quad \text{SCP} = \frac{\dot{Q}}{m_{\text{mem}}} = \frac{qA_{\text{LTR}}}{m_{\text{mem}}} \tag{22}$$

Here, m_{mem} is the mass fraction of the elastomer membrane contributing to the cooling process (i.e., touching the LTR, see Supplementary Note 9). Let us express *effective* and *intrinsic* COP and SCP in terms of temperature difference with background ΔT defined in eq. (15), using the last expressions in eq. (17). We also substitute α from eq. (14), to deal with directly measurable quantities only.

$$\begin{gathered} \text{COP}_{\text{effective}} = \frac{c_{\text{LTR}} m_{\text{LTR}}}{\dot{W}_{\text{in}}} \lambda(\Delta T_{\text{meas}} - \Delta T), \text{COP}_{\text{intrinsic}} = \frac{c_{\text{LTR}} m_{\text{LTR}}}{\dot{W}_{\text{in}}} \frac{\Delta T_{\text{meas}}}{\Delta T_{\text{mem}}} \lambda(\Delta T_{\text{mem}} - \Delta T) \\ \text{SCP} = \frac{\dot{W}_{\text{in}}}{m_{\text{mem}}} \text{COP} \end{gathered} \tag{23}$$

Supplementary Figures 4c-f show these, *directly and indirectly* measured *effective and intrinsic* heat pump characteristics for different experimental parameters and operating conditions. According to the comment after eq. (19), the *intrinsic* values also provide the dependences for the *ideal* system, because $\alpha\Delta T_{\text{mem}} = \lambda\Delta T_{\text{meas}}$. At the onset of the temperature curves $\Delta T(t=0) = 0$, and all three values – effective, intrinsic and ideal become the same:

$$\text{COP}_{\substack{\text{effective}\\ \text{intrinsic}\\ \text{ideal}}} = \frac{c_{\text{LTR}} m_{\text{LTR}}}{\dot{W}_{\text{in}}} \lambda\Delta T_{\text{meas}}, \text{SCP}_{\substack{\text{effective}\\ \text{intrinsic}\\ \text{ideal}}} = \frac{c_{\text{LTR}} m_{\text{LTR}}}{m_{\text{mem}}} \lambda\Delta T_{\text{meas}} \tag{24}$$

These initial, *maximum* values for COP and SCP are listed in Supplementary Table 1.

The thicker 180 µm membrane produces slightly larger ΔT_{meas} than the 140 µm membrane at the same operating conditions. Both membranes are made of the same material, and are expected to produce the same ΔT_{meas}. The discrepancy stems from the heat exchange dynamics between the elastomer and the LTR. ΔT_{meas} can be related to the ratio of intrinsic ideal and measured rate constants (eq. (14)):

$$\Delta T_{\text{meas}} = \frac{\alpha}{\alpha + \gamma} \Delta T_{\text{mem}} \tag{25}$$

The constant α, which describes the cooling energy transported per unit time, can be estimated as:

$$\alpha \sim \frac{(c_{\text{mem}} \Delta T_{\text{mem}} + \chi \Delta H) m_{\text{mem}}}{c_{\text{LTR}} m_{\text{LTR}}} \nu \tag{26}$$

Here, c_{mem} is the specific heat capacity of the elastomer membrane with density ρ, volume V and total mass $m_{\text{mem}} = \rho V$, χ is its crystallinity in the stretched state, ΔH is the crystallization enthalpy per unit mass and ν is the actuation frequency. The constant γ characterizes the parasitic heat transfer per unit time and can be estimated as:

$$\gamma \sim \frac{\eta A_{\text{LTR}}}{c_{\text{LTR}} m_{\text{LTR}}} \tag{27}$$

Here, η is the Newtonian heat exchange coefficient with the surroundings. The expression (27) is roughly constant and does not depend on the membrane mass m_{mem} (or other parameters), while the coefficient α in eq. (26) increases with it. Thus, the pre-factor ratio in eq. (25) increases with the membrane mass m_{mem}. For membranes with larger thickness H it becomes closer to 1, which brings the observed span ΔT_{meas} closer to its maximum possible value ΔT_{mem}.

In our analysis we assume a perfect recovery of the energy released in snap-back process. In general, we neglected parasitic effects, such as dissipative gas-dynamic energy losses, or heat exchange with the surrounding air during the fast, quasi-adiabatic snapping instabilities. The estimations justifying these assumptions are discussed in Supplementary Notes 7 and 8.

Supplementary Note 4. Simulation of the stretch distribution

In numerical studies we used the incompressible version of the Ogden hyperelastic model to describe the mechanical behaviour of the elastomer membrane, with the elastic energy density:

$$W(\lambda_1,\lambda_2,\lambda_3)=\sum_{p=1}^{3}\frac{2\mu_p}{\alpha_p^{\ 2}}(\lambda_1^{\alpha_p}+\lambda_2^{\alpha_p}+\lambda_3^{\alpha_p}-3) \tag{28}$$

Here, are the three principal stretches in the material. The material parameters, μ_p and α_p, are obtained from a tensile test with a specimen (50 mm, 4 mm, 0. $\mu_1 = 5.79$ kPa λ_i 14 mm) at a stretch speed of 50 mm/min. By fitting these experimental data, we obtain the following values: , $\mu_2 = 1.63\times10^{-3}$ kPa , $\mu_3 = 374.98$ kPa , $\alpha_1 = 4.43$, $\alpha_2 = 9.94$, $\alpha_3 = 1.26$. This corresponds to the linear shear modulus $\mu_0 = \sum_{p=1}^{3}\mu_p$ =380.77 kPa (ABAQUS 6.18 Documentation).

We use the software package, ABAQUS/Standard to simulate the inflation of the membrane in the experimental setup. The whole setup is considered as an axisymmetric 2D model; an oblate spheroidal HTR shape is used, with parameters listed in the Supplementary Note 9. The setup is simulated as rigid parts in the model. Membrane is modelled as MAX2 element, inflated by the pressure applied to its inner surface. There is no internal dissipation, or friction between the balloon and HTR/LTR.

Supplementary Fig. 5 shows inhomogeneous stretch distribution across the membrane due to clamping around its circumference. Stretch, crystallinity, and the associated temperature change are smaller at peripheral areas, which can be also seen in Fig. 3c and the associated Supplementary Video V2. However, with an idealized spherical membrane, or smaller clamping and inlet, or in other optimized geometries, these drawbacks can be avoided. This may further increase the efficiency of the setup about twice.

Supplementary Note 5. Elastomer actuator performance

We determined the electrical input power using the following formula:

$$P=\frac{1}{t_{\text{period}}}\int_0^{t_{\text{period}}}U(t)I(t)dt \tag{29}$$

Different values are due to different operating conditions in each experiment. The energy consumption of the actuator changes with slight variations in its preparation, the degree of inflation and the applied voltage amplitude. Actuators which were preconditioned with training cycles (see Materials and Methods) deliver the required pressure and volume difference at a lower voltage. The results in Supplementary Fig. 10 indicate, that the higher-pressure difference due to a thicker membrane or a smaller aperture, requires a lower energy input. This is surprising, and hints how to tweak operational parameters and design to increase efficiency. This was not further investigated here. The main electric power is consumed in the compliant electrode, which has high ohmic resistance. Although carbon grease has a good bulk conductivity (~100 Ohm), the multiple layers sandwiched within the actuator are thinned down and spread out considerably by pre-inflation, leading to a high resulting areal resistivity (not measured). Compliant electrodes with much higher conductivity have to be developed to allow for an electrically more efficient actuation. Measurements with different DEAs using $\mathrm{HTR_S}$ (Supplementary Fig. 10) and heat flow deduced from the Fig. 4d as in the Supplementary Note 3 resulted in highest COP values of about 0.1 for the near-optimal operating frequency of 1 Hz. These COP values are the result of the inefficiency of the electro-mechanical conversion by the DEA setup and manual DEA manufacturing. Significant optimization is possible in terms of DEA size, number, base DEA material, number of DEA-layers, the conductivity of compliant electrodes. All these quantities strongly affect the power uptake of the DEA and system's operation. Practical implementations can also use other commercial electro-mechanical transducers with much higher energy conversion efficiency.

Supplementary Note 6. Cycling lifetime and its optimization

The lifetime of the actuated membranes is crucial for practical realizations. The cycling fatigue properties of NR are well researched. The crystallization significantly prolongs fatigue lifetime due to the stabilizing influence of SIC on crack growth[44]. Resent work on the subject[45] shows stable results up to ~10^6 cycles (at room temperatures, where we operate, see Figs. 5, 7 there and references therein). The authors of ref.[46] studied the fatigue effects in NR, deliberately targeting elastocaloric applications. They found, that the cycling performance in the amorphous stretch region 1-4 was unsatisfactory, while it improves in the SIC region of (1D) stretch 5-8, and especially 3-6, where 1.7×10^5 cycles are demonstrated (with some degradation in elastocaloric performance). Similarly, the authors of ref.[47] used oscillatory 1D stretch in the interval $5 < \lambda < 6$ only, with correspondingly smaller temperature changes $\Delta T = 2\,\mathrm{K}$. Such stretch values reasonably overlap with the region, where our device operates.

Our readily available commercial off-the shelve samples are not optimized for the task at hand. Also, the initial planar membrane geometry is not ideal for spherical inflation. Inhomogeneous stretch and stress distributions across the inflated membrane (see Supplementary Note 4 and Supplementary Fig. 5) facilitate rupture on the defects present in the material (see Supplementary Fig. 6). When inflation starts from small stretches in the amorphous range, these defects result in a typical lifetime of ~500 cycles. If the cycling proceeds from larger finite stretch values, avoiding fully amorphous range, longer lifetimes beyond 1000 cycles are demonstrated, as shown in the Supplementary Fig. 7.

For better reliability, one should make stretch more homogeneous across the membrane and adjust the sizes of the HTR, and the LTR to increase cycling lifetime. A possible realization of such a device is shown schematically in Supplementary Fig. 8. It contains several modifications for future, improved designs: 1. A more spherical geometry using high-quality rubber membrane custom-cast into spherical shape. This reduces stretch inhomogeneities and the influence of defects; 2. A larger LTR and smaller HTR, resulting in smaller stretch range, to avoid both overstretching and amorphous range to increase the cycling lifetime; 3. A fluidic heat exchanger, which reduces the parasitic heating of the LTR, thus better utilizing the intrinsic adiabatic temperature change; 4. A compact electro-mechanical (or alternative) transducer with high conversion efficiency.

We decided against such schemes, as they would significantly increase the complexity of our prototype and somewhat conceal the fundamental principles discussed here.

From our preliminary findings, as well as from the reported cycling fatigue properties of NR, we expect significant lifetime improvements for spherical membranes with a homogeneous stretch distribution, custom-cast by elastomer manufacturers from homogeneous high-quality rubbers with tailored material properties.

Supplementary Note 7. Heat exchange with the surrounding air during quasi-adiabatic snapping

Heat exchange with the surrounding during snapping can be estimated from the heat equation. For two semi-infinite solids in thermal contact, with initial temperature $T_{\mathrm{mem}} = T_0, x > 0$ ("rubber"), and $T_{\mathrm{air}} = 0, x < 0$ ("air"), the propagation of heat waves in both directions is given by the equations (2.15.5-6) in ref.[48] The temperature exactly at the border remains constant, and equal to $\frac{T(0)}{T_0} = \frac{\sqrt{K_{\mathrm{mem}} c_{\mathrm{mem}} \rho}}{\sqrt{K_{\mathrm{mem}} c_{\mathrm{mem}} \rho} + \sqrt{K_{\mathrm{air}} c_{\mathrm{air}} \rho_{\mathrm{air}}}} \approx 0.988$. This means, that within about 1% it remains equal to the initial temperature of the "thermally denser" body, in our case rubber. Parameters used in estimations are listed in the Supplementary Note 9. After the thermal time for the membrane $t_{\mathrm{mem}} \sim h^2 / 4D_{\mathrm{mem}} \sim 4\,\mathrm{ms}$ (for a 35 μm membrane) the temperature in the membrane acquires a quasi-stationary profile. Here, the initial rubber membrane thickness is 140-180 μm, but it quickly decreases to below 10 μm in the course of snap-through. The representative thickness of 35 μm corresponds to the lateral stretch $\lambda = 2$, reached early in the inflation stage. Its further evolution is governed by the energy exchange with the air, and for the area A (which cancels from the final result) it can be estimated as follows.

$$\begin{gathered} c_{\mathrm{mem}}\rho h A\dot{T} \sim -2AK_{\mathrm{air}}\frac{\partial T_{\mathrm{air}}}{\partial z} \sim -2AK_{\mathrm{air}}\frac{T}{2\sqrt{D_{\mathrm{air}}t}} \Rightarrow \\ \frac{dT}{T} \sim -\frac{\sqrt{K_{\mathrm{air}}c_{\mathrm{air}}\rho_{\mathrm{air}}}}{c_{\mathrm{mem}}\rho h}\frac{dt}{\sqrt{t}} \qquad \Rightarrow T \sim T_0 \exp\left(-\frac{2\sqrt{K_{\mathrm{air}}c_{\mathrm{air}}\rho_{\mathrm{air}}t}}{c_{\mathrm{mem}}\rho h}\right) \end{gathered} \tag{30}$$

The time constant in this expression is of the order of $\tau \approx \frac{(c_{\mathrm{mem}}\rho h)^2}{4K_{\mathrm{air}}c_{\mathrm{air}}\rho_{\mathrm{air}}} \sim 28\,\mathrm{s}$. Because the expansion/contraction stages are ~300 time shorter (see Fig. 2b), the temperature change due to thermal contact with the air is negligible, and the adiabatic approximation is justified. The exact temperature profile within the membrane, or semi-empirical convective Newtonian heat exchange coefficients modify numerical pre-factors in these estimations, but do not change the conclusions.

Similar considerations can be used for the energy exchange with the reservoirs LTR and HTR. Here, the time constants from eq. (30) $\tau_{\mathrm{R}} \sim 10^{-5}\,\mathrm{to}\,10^{-7}\,\mathrm{s}$, due to much larger denominator and thinner membrane on the HTR. The relevant time becomes the thermal time of the membrane, which is at most $t_{\mathrm{mem}} \sim 64\,\mathrm{ms}$ for the unstretched membrane on the LTR. As the membrane remains in contact with the reservoirs for 0.2-1 s, the temperature appropriately equilibrates with them.

Supplementary Note 8. Estimation of the gas-dynamic frictional energy losses

Gas-dynamics at the inlet/outlet affects the operation of the heat pump. We investigated this in a separate set of experiments (not presented), by varying the outlet duct diameter from 1 to 40 mm. The measured p-V hysteresis stabilized for diameters below 3 mm, which is still fast enough for the adiabatic approximation to hold (~ 100 ms, Fig. 2b), as discussed in the Supplementary Note 7. The inflation is slower than the deflation (Fig. 2b), so that gas dynamic effects are even smaller there. Let us estimate the contribution of the viscous dissipation onto the key eq. (10). We use various relations from ref.[49], omit dimensionless coefficients of the order of unity, and assume that gas flow has characteristic velocity v and spatial scale R (they will be further discussed below). The volumetric dissipative source term is $Q \sim \eta(v/R)^2$. The dynamic viscosity η is related to the kinematic one ν, and further to the molecular mean free path $\lambda \approx 70\,\mathrm{nm}$ and thermal velocity, which is comparable with the sound velocity: $\eta \sim \rho_{\mathrm{air}}\nu \sim \rho_{\mathrm{air}}\lambda c_{\mathrm{sound}}$. The total pressure is of the order of $p \sim \rho_{\mathrm{air}} c_{\mathrm{sound}}^2$. Equation (10) deals with the *o*verpressure Δp, while the air itself is close to the normal conditions, so that the full pressure p should be used for the determination of the molecular mean free path and other gas parameters. Thus, the comparison of the total frictional energy dissipation over the inflation/deflation time t with the inflation work in eq. (10) $\int p dV_{\mathrm{b}} \sim \Delta p V_{\mathrm{b}}$ takes on the following form:

$$\begin{aligned} QV_{\mathrm{b}}t \sim \rho_{\mathrm{air}}\lambda c_{\mathrm{sound}}(v/R)^2 V_{\mathrm{b}}t \sim p\lambda(v/R)^2 V_{\mathrm{b}}t/c_{\mathrm{sound}} \quad &\vee \quad \Delta p V_{\mathrm{b}} \quad \Rightarrow \\ \frac{p}{\Delta p}\frac{\lambda v}{Rc_{\mathrm{sound}}}\frac{vt}{R} \quad &\vee \quad 1 \end{aligned} \tag{31}$$

In our experiments $p/\Delta p \sim 10$; for the balloon the ratio $vt/R \sim 1$ effectively cancels; and the overall ratio in eq. (31) becomes $10\lambda / c_{\mathrm{sound}}t \sim 2\times10^{-8} \ll 1$. More critical is the dissipation in the outlet duct. Its length is $L = 1.5\,\mathrm{cm}$, and the smallest used radius is $R = 0.15\,\mathrm{cm}$, so that simple flow estimations produce velocities comparable with the speed of sound, $v/c_{sound} \le 1$. In this case, the dissipative losses should be calculated for the volume of the outlet channel $V_{\mathrm{out}} = \pi R^2 L \ll V_{\mathrm{b}}$, resulting in the overall ratio $\frac{p}{\Delta p}\frac{\lambda}{R}\frac{c_{\mathrm{sound}}t}{R}\frac{V_{\mathrm{out}}}{V_{\mathrm{b}}} \sim 3\times10^{-3} \ll 1$. More technical approaches, e.g., based on the viscous losses in the cylindrical Poiseuille flow, or the Darcy-Weisbach factor with Borda-Carnot assumptions about the dissipated energy upon a sudden contraction/expansion of a cylindrical duct lead to comparable estimations (Table 7.5-1 in ref.[50], for tabulated values for compressible flow see L.1.2.1 and L.1.3.1-3 in ref.[51]). The pressure was measured in the pressure vessel, directly connected to the balloon via wide openings (Supplementary Fig. 1), so that any pressure losses on the inlet and outlet valves are excluded from the consideration. The flow velocity in the pressure vessel itself is much smaller, and the dissipation there is negligible, due to quadratic dependence on v in eq. (31). Moreover, we deliberately used pressure reservoirs to reduce the operating pressure differences and related parasitic and dissipative effects.

Supplementary Note 9. Parameters used in calculations

Here we list various thermophysical constants and setup parameters used in calculations throughout the Main Text, Methods and Supplementary Notes.

Ambient air.

Density $\rho_{\text{air}} = 1.2\times10^{-3}\,\text{g/cm}^3$, specific heat capacity $c_{\text{air}}=1\,\text{J/g K}$, thermal conductivity $K_{\text{air}}=2.6\times10^{-4}\,\text{W/cm K}$, thermal diffusivity $D_{\text{air}}=0.217\,\text{cm}^2/\text{s}$, reference ambient temperature used in eq. (11), $T_0=293\,\text{K}$.

NR elastomer membrane.

Density $\rho = 0.93\,\text{g/cm}^3$, specific heat capacity $c_{\text{mem}}=1.83\,\text{J/g K}$, thermal conductivity $K_{\text{mem}} = 1.3\times10^{-3}\,\text{W/cm K}$, thermal diffusivity $D_{\text{mem}}=7.6\times10^{-4}\,\text{cm}^2/\text{s}$, crystallization enthalpy $\Delta H = 38\,\text{J/g}$ [30], (65.3 J/g is reported in melts).

Membrane parameters.

Geometry within the aperture, used in balloon expansion calculations (eq. (10)): radius $r = 1.5\,\text{cm}$, volume $V = 0.099\,\text{cm}^3$, m=$0.092\,\text{g}$ (the latter two for thickness $H = 140\,\mu\text{m}$). Effective recalculated unstretched membrane radius on the LTR is ~0.95 cm, and measured mass, used in thermal calculations m_{mem}[g]= 0.036 ($H = 140\,\mu\text{m}$), 0.049 ($H = 180\,\mu\text{m}$).

Thermal reservoirs properties.

LTR: spherical cap radius $r_{\text{LTR}} = 1\,\text{cm}$, height $h_{\text{LTR}} = 0.3\,\text{cm}$, area $A_{\text{LTR}} = 3.42\,\text{cm}^2$, mass $m_{\text{LTR}}=1.9\,\text{g}$, specific heat capacity $c_{\text{LTR}}=0.9\,\text{J/g K}$.

HTR (small (S) and large (L)): spheroidal radius r_{HTR}[cm]=3.3 (S), 3.85 (L), depth h_{HTR}[cm]=3 (S), 3.3 (L).

Balloon properties on both HTR, small (S) and large (L):

Balloon volume $V_{\text{b}}[\text{cm}^3] = 115$ (S), 200 (L).

Inflation/deflation pressure work integrals [J] in eq. (5) from the main text and eq. (10):

$\int_0^{V_{\max}} p_{\text{infl}} dV_{\text{b}} = 0.79$, $\int_0^{V_{\max}} p_{\text{defl}} dV_{\text{b}} = 0.71$, (S), $\int_0^{V_{\max}} p_{\text{infl}} dV_{\text{b}} = 1.41$, $\int_0^{V_{\max}} p_{\text{defl}} dV_{\text{b}} = 1.1$, (L).

Maximum membrane crystallinity obtained from eq. (10), $\chi = 0.23$ (S), 0.27 (L).

Fitting parameters used in Supplementary Figs. 4b-f.

Intrinsic membrane temperature change, defined below the eq. (11), measured with IR camera (Fig. 3e), $\Delta T_{\mathrm{mem}}[\mathrm{K}]$=11 (HTR$_\mathrm{S}$), 14.1 (HTR$_\mathrm{L}$).

Effective (asymptotic) LTR temperature span, obtained from the fit of the measured temperature cooling curves by eq. (12): $\Delta T_{\mathrm{meas}}[\mathrm{K}] = 8.0$ (b), 4.5 (c), 4.7 (d), 7.1 (e), 7.4 (f).

Decay constants.

Intrinsic, $\alpha[\mathrm{s}^{-1}]$ in eq. (14): 0.036 (b), 0.011 (c), 0.019 (d), 0.022 (e), 0.029 (f)
Parasitic, $\gamma[\mathrm{s}^{-1}]$ in eq. (14): 0.027 (b), 0.017 (c), 0.026 (d), 0.022 (e), 0.026 (f)
Effective *measured* $\lambda[\mathrm{s}^{-1}]$ in eq. (12): 0.064 (b), 0.028 (c), 0.045 (d), 0.044 (e), 0.055 (f)

Supplementary Figures

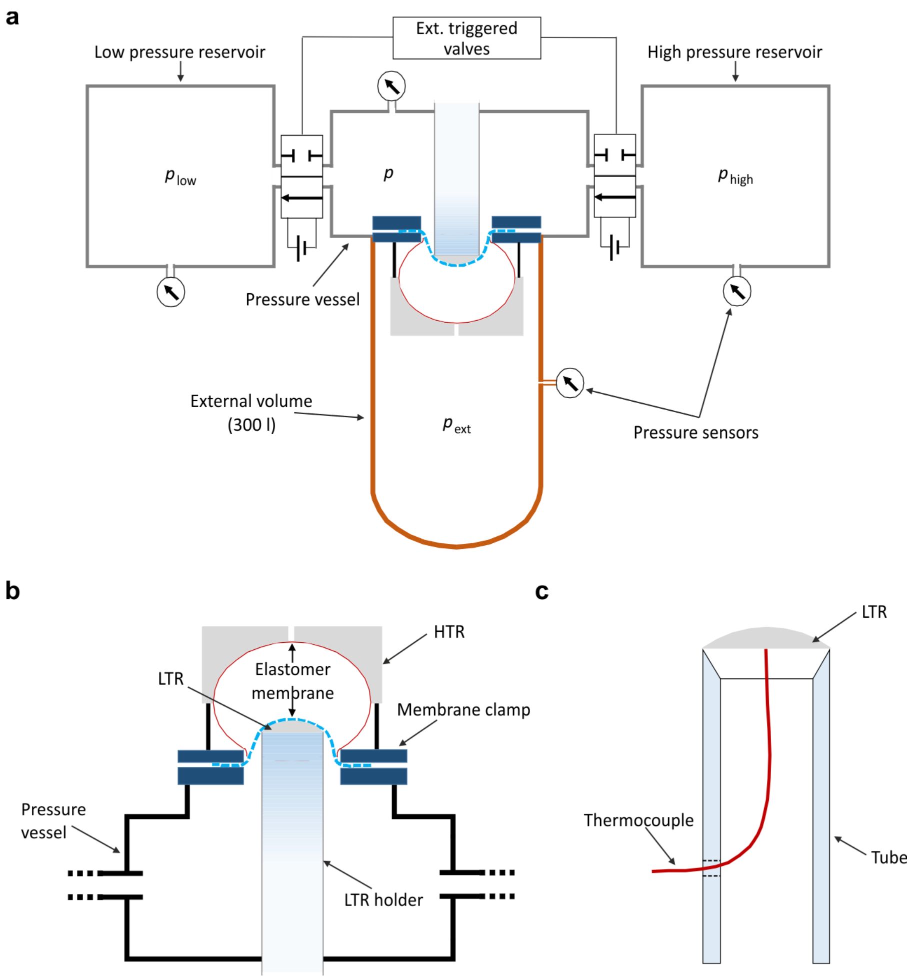

Supplementary Figure 1. Experimental setup. **(a)** Overall setup including the high (p_{high}) and low (p_{low}) pressure reservoirs, the external volume (p_{ext}) and the pressure vessel (p). **(b)** Detailed illustration of the pressure vessel connected to the LTR and HTR as well as to the clamp fixating the cooling elastomer membrane. The clamp had an inner circular aperture of 30 mm diameter. The LTR holder was fixed on the rear side of the pressure vessel within a pneumatically sealed sliding mechanism. This mechanism was used to move the holder upwards after fixation of the membrane in order to establish full contact. **(c)** Detailed illustration of the LTR holder. The LTR was mounted on a plastic tube, which had its walls thinned at the contact site to minimize parasitic heat flow. A thermocouple is inserted via a tiny hole into the LTR holder and fixed at the bottom of the LTR to measure the temperature decrease. Good thermal contact was ensured applying heat conductive paste at the contact area of thermocouple and the LTR.

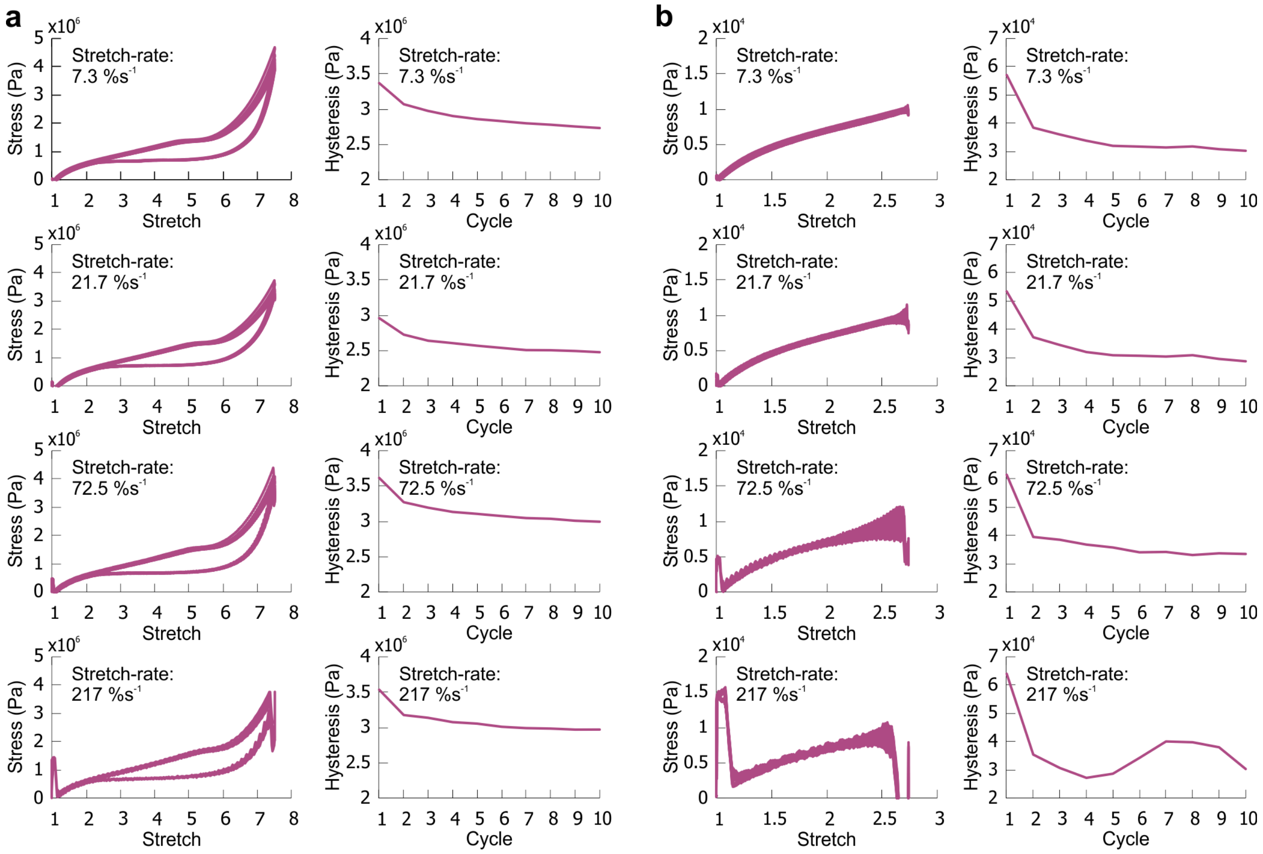

Supplementary Figure 2. Uniaxial cyclic tensile tests. (a) Maximum stretch of 7.5 demonstrates large hysteresis due to SIC. Left columns are the stress-stretch relationships for cyclic deformation at different rates indicated in the legend. Right columns show the area within the hysteretic curve for each cycle. Hysteresis values decrease due to Mullins effect, and stabilize after 5-10 cycles. No holding time between the stretch, contraction and successive cycles. There is no noticeable difference between the slowest and fastest cycling (178 vs. 6 s/cycle). **(b)** Maximum stretch 2.7 is shown for comparison, it demonstrates virtually no hysteresis.

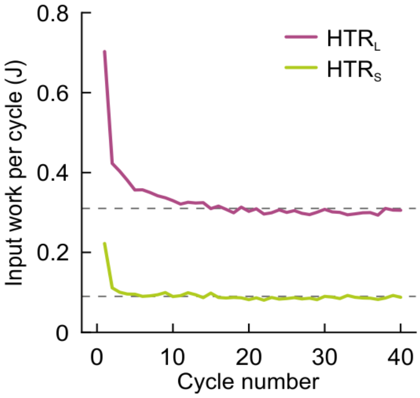

Supplementary Figure 3. Hysteresis per cycle of the inflated elastomer membrane (thickness 140 µm). We measured the input energy consumption of balloon actuation and determined the equilibrium value for both HTR sizes (dashed lines) at frequency 0.9 Hz (for experimental details see Methods section "*p*-V measurements"). As opposed to Supplementary Fig. 2, here the stretch was applied biaxially by inflating the membrane. Also, the hysteresis is defined in terms of total energy from *p*-V diagram (gas pressure and volume), whereas the hysteresis in Supplementary Fig. 2 is given in energy density units of Pa=J/m^3 deduced from the uniaxial tensile test. Dividing energy from Supplementary Fig. 2 by the volume of the elastomer membrane V (not the balloon volume V_b), we obtain values ~4×10^6 Pa, which are consistent with the hysteresis from Supplementary Fig. 2. The input work of the first ~40 cycles is displayed. Due to the Mullins effect, the required energy for the initial ~5 cycles is relatively high, but quickly decreases and stabilizes around a certain constant value. Due to the quick convergence, we used these constant values (mean of all cycles > 10) to compute heat pump characteristics.

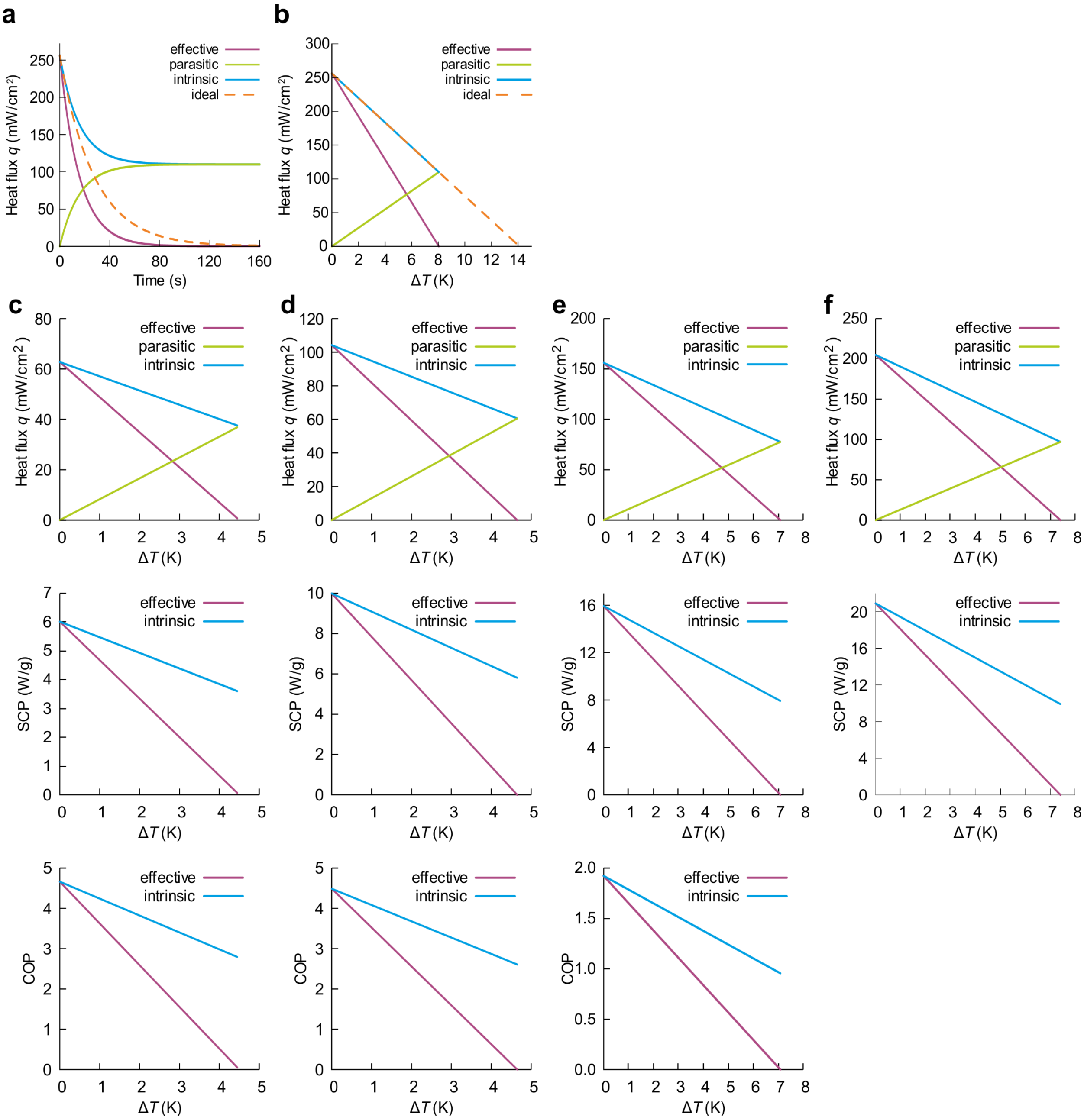

Supplementary Figure 4. Contributions to heat-flux. (a-b**)** An extended version of Fig. 2f (membrane thickness: 180 µm, frequency *f* = 1.1 Hz with HTR$_L$). **(a)** Heat flux vs. time. **(b)** Heat flux vs. temperature difference. **(c**-f**)** Measured and simulated heat pump characteristics for different operating conditions (membrane thickness: 140 µm). **(c)** *f* = 0.5 Hz with HTR$_S$. **(d)** *f* = 0.9 Hz with HTR$_S$. **(e)**, *f* = 0.9 Hz with HTR$_L$. **(f)** *f* = 1.1 Hz with HTR$_L$.

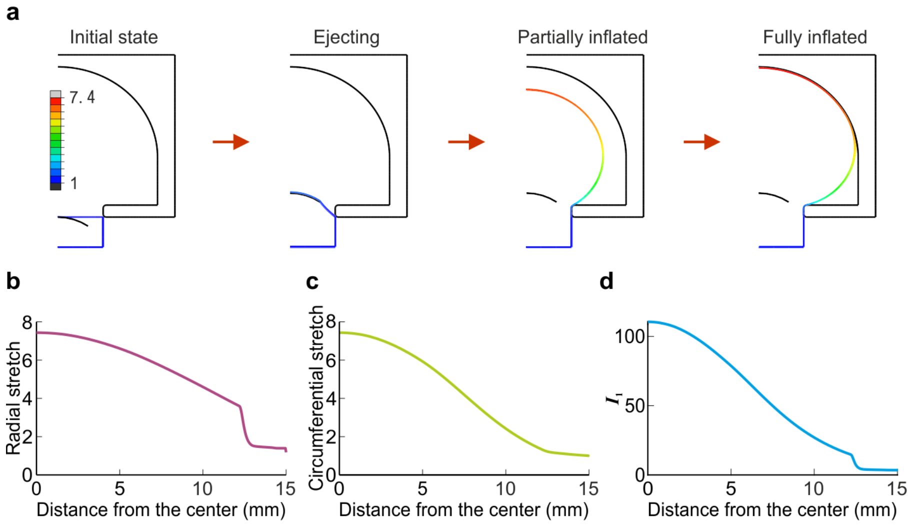

Supplementary Figure 5. Simulated inflation of the elastomer membrane. (a) Snapshots of different inflation stages in a setup using HTR$_\mathrm{S}$ (see Supplementary Note 9) and an aperture of 30 mm. The colour bar shows the radial stretch (see panel b), the black lines represent the mechanical constraints. **(b-d)** Distribution of stretch for the fully inflated NR (last panel in a) The results are projected on the aperture area. The distance from the centre of the membrane is in the unstretched reference configuration. (b) Radial stretch. (c) Circumferential stretch. (d) First stretch invariant, $I_1 = \sum_i \lambda_i^2$.

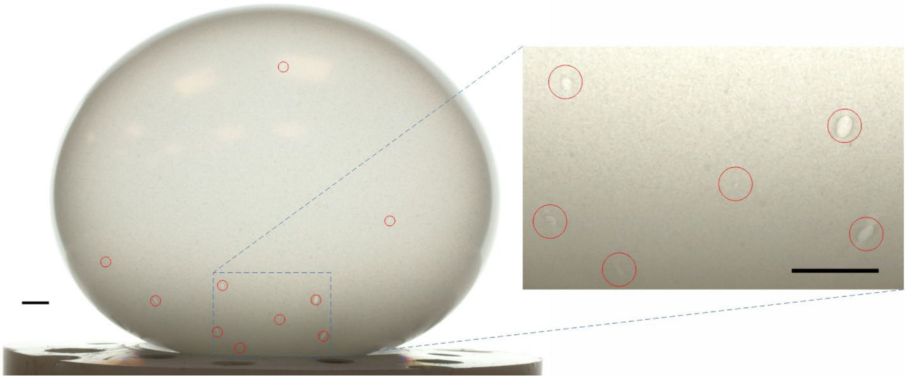

Supplementary Figure 6. Defects and stretch inhomogeneity. The inset shows a magnified region with several visible defects. Scale bar is 1 cm.

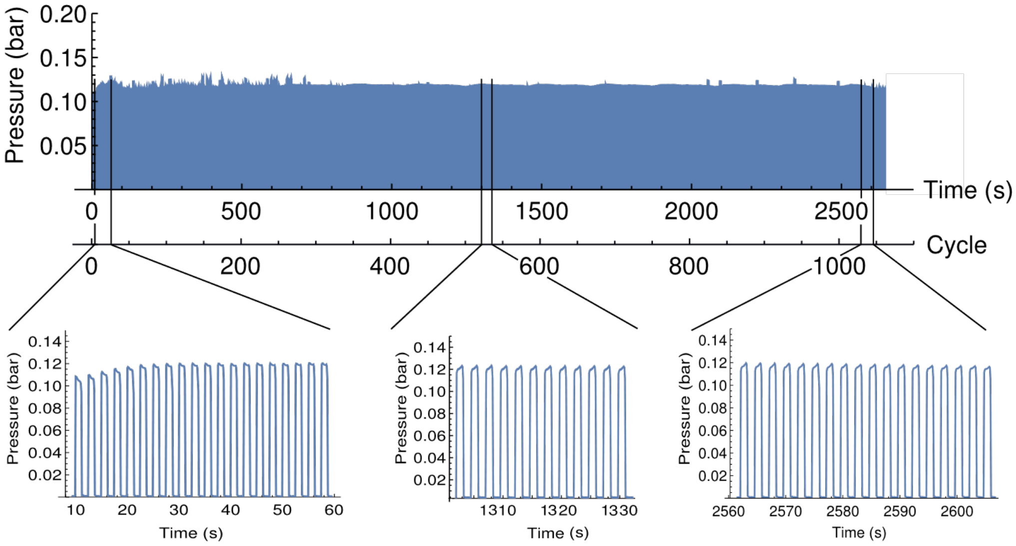

Supplementary Figure 7. Cycling lifetime test of an inflated membrane. The test is operating at 0.4 Hz for more than 1000 cycles in the stretch range $\lambda_{\min} < \lambda < \lambda_{\max}$. Minimum stretch was adjusted by the position of the LTR (with respect to the HTR) and its value (in the central region) $\lambda_{\min} \approx 3.7$ is determined from the distance change between the reference ink marks. The central stretch $\lambda_{\max} \approx 7.4$ is defined by the HTRs size.

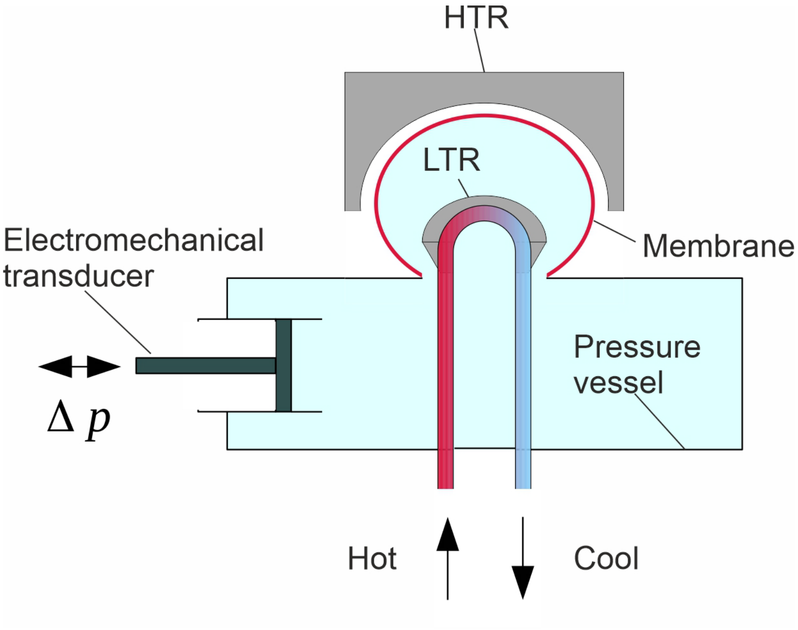

Supplementary Figure 8. Schematic with key components of a practical device. Our NR based electrocaloric cooling system can be built in compact form factors; essential are an HTR and LTR, the rubber membrane, a pressure vessel of about 5-10 times the volume displaced by the snapping operation, and a transducer creating small, periodic pressure variations (~2 kPa).

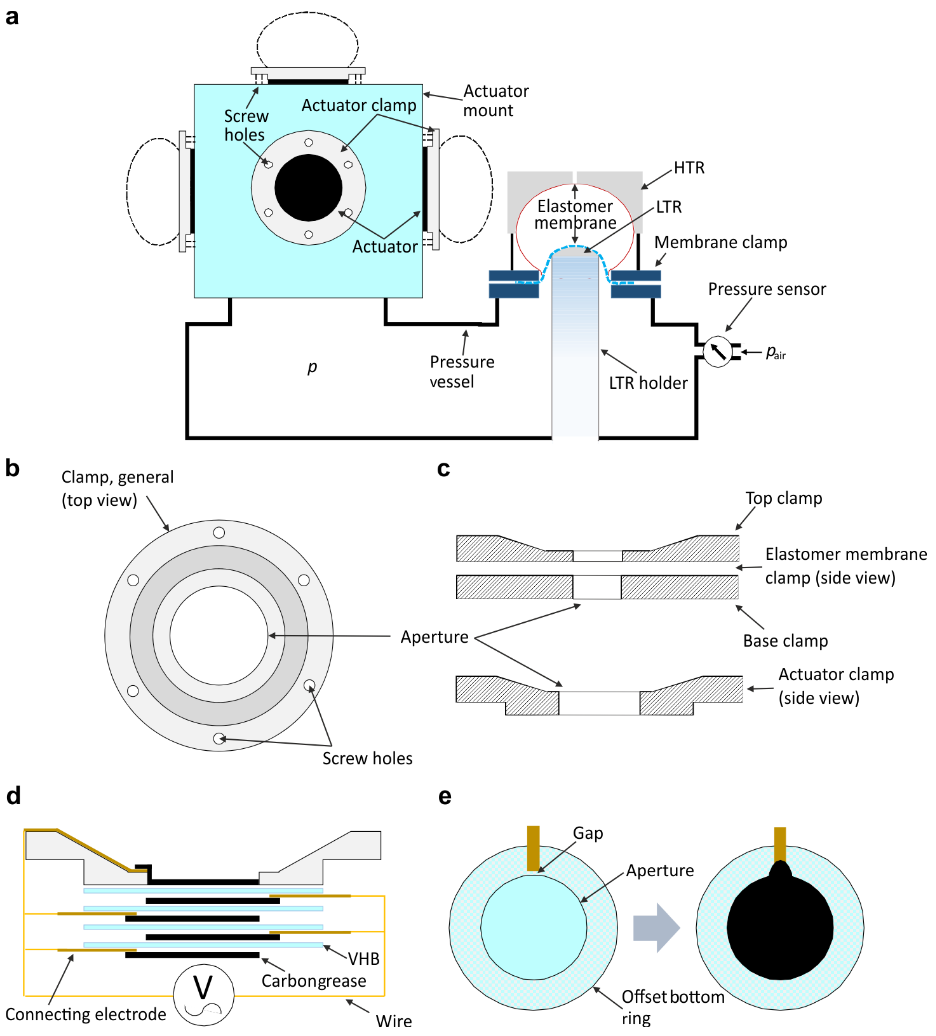

Supplementary Figure 9. Schematic illustration of the actuator setup, the fixating clamps and the DEA design. **(a)** The actuator part is connected to the geCC heat-pump via the pressure vessel. Each of the five actuators is placed on one side of a cubic Plexiglas actuator mount (blue area). The single DEAs are clamped and fixated with screws to the actuator mount. At the sixth cubic surface the pressure vessel is attached. The cuboid mount has inner dimensions of 120×120×130 mm^3 and is made out of Plexiglas with a thickness of 15 mm. The circular apertures for the DEAs measure 45 mm in diameter. The actuator clamps are 3D-printed with ABS. **(b)** They have an outer diameter of 90 mm, a total thickness of 6 mm and an aperture of 45 mm. The inner region has a diameter of 56 mm. On the top side the clamp thins down towards the centre to a height of 2 mm. The fixating clamps of the elastomer membrane as well as of the DEAs have the same shape on the top side. **(c)** Top: The DEA VHB membrane clamp consists of two components which are mounted on top of the pressure vessel. Bottom: The actuator clamp has an offset bottom to facilitate attachment of the actuator stack. The offset bottom has a diameter of 70 mm and a thickness of 2 mm. The actuator clamp is directly attached to the actuator mount and hence only consists of one component. **(d)** Side view of a four-layer actuator stack. The illustration shows the attachment to the actuator clamp and the wiring required for operation. **(e)** Rear view of the actuator clamp during actuator assembly. The schematic shows the positioning of the connecting electrode and the correct distribution of carbon grease. In order to avoid any perforation of the inflated actuator by sharp edges, the inner end of the strip must never be placed inside the aperture, but close before (Gap).

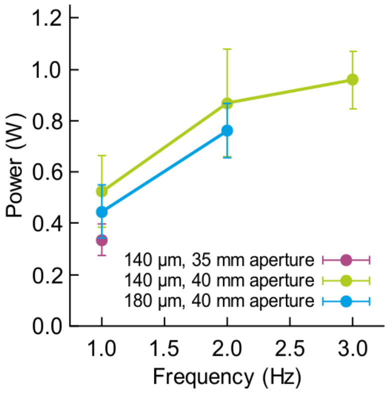

Supplementary Figure 10. Electrical input power of the elastomer actuator. The mean power consumption of actuation for different membrane thicknesses, apertures and actuation frequencies. The error bars show standard deviation from the mean values. The number of samples *n* was as follows: 140 µm, 35mm: *n*=3 (1 Hz); 140 µm, 40 mm: *n*=7 (1 Hz), 7 (2 Hz), 4 (3 Hz); 180 µm, 40 mm: *n*=4 (1 Hz), 4 (2 Hz).

Supplementary Table 1. Performance comparison of cooling systems based on different caloric effects†.

Category	Material	Reference	COP	Temperature change (K)	Heat flux (mW/cm^2)	Loading cycles	SCP (W/g)
Magneto-	Metal	[52]	25.22	3^{**}	-	1.41×10^{2}	0.02
	Metal	[53]	2	7^{**}	-	-	0.039
	Metal	[54]	9.5	$23^{\#}$	-	-	0.166
	Metal	[55]	2.5	$11.9^{**\&}$	-	-	0.17
	Metal	[56]	10	$29^{**\&}$	-	-	0.9
	Metal	[57]	1.23	16.8^{**}	-	-	0.948
	Metal	[58]	1.9	12^{**}	-	-	2
Baro-	Plastic	[59]	-	$50^{\#}$	-	-	-
	Plastic	[60]	-	$62^{\#}$	-	-	-
	Soft Elastomer	[61]	9	$9^{\#}$	-	-	-
Electro-	Ceramics	[62]	14	0.25^{**}	-	-	-
	Ceramics	[63]	2.7	5.2^{**}	135	-	0.007^{*}
	Ceramics	[64]	-	13^{**}	-	-	0.85
Elasto-	Metal	[65]	4.5	$11^{\#}$	-	1.2×10^{4}	-
	Metal	[66]	-	$19.9^{\#}$	-	5.5×10^{3}	-
	Metal	[67]	20	$27^{\#}$	-	1×10^{6}	-
	Soft Elastomer	[68]	8.5	$19.1^{\#}$	-	7.5×10^{2}	-
	Metal	[69]	6.0	28^{**}	-	4×10^{2}	0.777
	Metal	[70]	3.5	15.3^{**}	-	2×10^{3}	0.8
	Plastic	[71]	13	$1.4^{\#}$	29.7	3×10^{4}	2.8
	Metal	[72]	4.9	$20^{\#}$	-	1×10^{2}	4.5
	Metal	[73]	3	13^{**}	-	-	7.7
	Metal	[74]	6	20^{**}	-	-	18
	Soft Elastomer	**This work**	**4.7**	**7.9^{**}**	**256**	**1×10^{3}**	**20.9**

† Maximum values taken from literature.

* Calculated for the whole device, without power supply.

** Temperature span between the hot and cold sides of a device

$^{\#}$ Adiabatic temperature change of the working material

$^{\&}$ No thermal load

- No data available

Supplementary References

1 Albouy, P.-A. & Sotta, P. in *Polymer Crystallization II: From Chain Microstructure to Processing* (eds Finizia Auriemma, Giovanni Carlo Alfonso, & Claudio de Rosa) 167-205 (Springer International Publishing, 2017).

2 Huneau, B., Le Cam, J. B., Marco, Y. & Verron, E. in *11th European Conference on Constitutive Models for Rubber.* 620.

3 Albouy, P. A. & Sotta, P. Strain-Induced Crystallization in Natural Rubber. *Polymer Crystallization Ii: From Chain Microstructure to Processing* **277**, 167-205, doi:10.1007/12_2015_328 (2017).

4 Huneau, B. Strain-Induced Crystallization of Natural Rubber: A Review of X-Ray Diffraction Investigations. *Rubber Chem. Technol.* **84**, 425-452, doi:10.5254/1.3601131 (2011).

5 Chen, P. Z. *et al.* In situ characterization of strain-induced crystallization of natural rubber by synchrotron radiation wide-angle X-ray diffraction: construction of a crystal network at low temperatures. *Soft Matter* **15**, 734-743, doi:10.1039/c8sm02126k (2019).

6 Miyamoto, Y., Yamao, H. & Sekimoto, K. Crystallization and melting of polyisoprene rubber under uniaxial deformation. *Macromolecules* **36**, 6462-6471, doi:10.1021/ma0342877 (2003).

7 Guo, Q., Zairi, F. & Guo, X. L. Thermodynamics and mechanics of stretch-induced crystallization in rubbers. *Physical Review E* **97**, 052501, doi:ARTN 052501, 10.1103/PhysRevE.97.052501 (2018).

8 Guo, Q., Zairi, F. & Guo, X. L. A thermo-viscoelastic-damage constitutive model for cyclically loaded rubbers. Part II: Experimental studies and parameter identification. *Int. J. Plast.* **101**, 58-73, doi:10.1016/j.ijplas.2017.10.009 (2018).

9 Plagge, J. & Kluppel, M. Mullins effect revisited: Relaxation, recovery and high-strain damage. *Materials Today Communications* **20**, 100588, doi:UNSP 100588, 10.1016/j.mtcomm.2019.100588 (2019).

10 Plagge, J. & Kluppel, M. Determining strain-induced crystallization of natural rubber composites by combined thermography and stress-strain measurements. *Polym. Test.* **66**, 87-93, doi:10.1016/j.polymertesting.2017.12.021 (2018).

11 Le Gac, P. Y., Albouy, P. A. & Sotta, P. Strain-induced crystallization in a carbon-black filled polychloroprene rubber: Kinetics and mechanical cycling. *Polymer* **173**, 158-165, doi:10.1016/j.polymer.2019.04.019 (2019).

12 Le Gac, P. Y., Albouy, P. A. & Petermann, D. Strain-induced crystallization in an unfilled polychloroprene rubber: Kinetics and mechanical cycling. *Polymer* **142**, 209-217, doi:10.1016/j.polymer.2018.03.034 (2018).

13 Guo, Q., Zairi, F. & Guo, X. L. A thermo-viscoelastic-damage constitutive model for cyclically loaded rubbers. Part I: Model formulation and numerical examples. *Int. J. Plast.* **101**, 106-124, doi:10.1016/j.ijplas.2017.10.011 (2018).

14 Xie, Z. J., Sebald, G. & Guyomar, D. Comparison of elastocaloric effect of natural rubber with other caloric effects on different-scale cooling application cases. *Appl. Therm. Eng.* **111**, 914-926, doi:10.1016/j.applthermaleng.2016.09.164 (2017).

15 Xie, Z. J., Wei, C., Guyomar, D. & Sebald, G. Validity of Flory's model for describing equilibrium strain-induced crystallization (SIC) and thermal behavior in natural rubber. *Polymer* **103**, 41-45, doi:10.1016/j.polymer.2016.09.038 (2016).

16 Xie, Z. J., Sebald, G. & Guyomar, D. Comparison of direct and indirect measurement of the elastocaloric effect in natural rubber. *Appl. Phys. Lett.* **108**, 041901, doi:Artn 041901, 10.1063/1.4940378 (2016).

17 Xie, Z. J., Sebald, G. & Guyomar, D. Elastocaloric effect dependence on pre-elongation in natural rubber. *Appl. Phys. Lett.* **107**, 081905, doi:Artn 081905, 10.1063/1.4929395 (2015).

18 Le Cam, J. B. Strain-induced crystallization in rubber: A new measurement technique. *Strain* **54**, e12256, doi:ARTN e12256, 10.1111/str.12256 (2018).

19 Le Cam, J. B. Energy storage due to strain-induced crystallization in natural rubber: The physical origin of the mechanical hysteresis. *Polymer* **127**, 166-173, doi:10.1016/j.polymer.2017.08.059 (2017).

20 Samaca Martinez, J. R., Le Cam, J. B., Balandraud, X., Toussaint, E. & Caillard, J. Mechanisms of deformation in crystallizable natural rubber. Part 2: Quantitative calorimetric analysis. *Polymer* **54**, 2727-2736, doi:10.1016/j.polymer.2013.03.012 (2013).

21 Samaca Martinez, J. R., Le Cam, J. B., Balandraud, X., Toussaint, E. & Caillard, J. Mechanisms of deformation in crystallizable natural rubber. Part 1: Thermal characterization. *Polymer* **54**, 2717-2726, doi:10.1016/j.polymer.2013.03.011 (2013).

22 Flory, P. J. Thermodynamics of Crystallization in High Polymers .1. Crystallization Induced by Stretching. *J. Chem. Phys.* **15**, 397-408, doi:Doi 10.1063/1.1746537 (1947).

23 Behnke, R., Berger, T. & Kaliske, M. Numerical modeling of time- and temperature-dependent strain-induced crystallization in rubber. *Int. J. Solids Struct.* **141**, 15-34, doi:10.1016/j.ijsolstr.2018.01.034 (2018).

24 Rastak, R. & Linder, C. A non-affine micro-macro approach to strain-crystallizing rubber-like materials. *J. Mech. Phys. Solids* **111**, 67-99, doi:10.1016/j.jmps.2017.10.007 (2018).

25 Nateghi, A., Dal, H., Keip, M. A. & Miehe, C. An affine microsphere approach to modeling strain-induced crystallization in rubbery polymers. *Continuum Mech. Thermodyn.* **30**, 485-507, doi:10.1007/s00161-017-0612-8 (2018).

26 Guilie, J., Le, T. N. & Le Tallec, P. Micro-sphere model for strain-induced crystallisation and three-dimensional applications. *J. Mech. Phys. Solids* **81**, 58-74, doi:10.1016/j.jmps.2015.05.004 (2015).

27 Mistry, S. J. & Govindjee, S. A micro-mechanically based continuum model for strain-induced crystallization in natural rubber. *Int. J. Solids Struct.* **51**, 530-539, doi:10.1016/j.ijsolstr.2013.10.027 (2014).

28 Kroon, M. A constitutive model for strain-crystallising Rubber-like materials. *Mech. Mater.* **42**, 873-885, doi:10.1016/j.mechmat.2010.07.008 (2010).

29 Khiêm, V. N. & Itskov, M. Analytical network-averaging of the tube model: Strain-induced crystallization in natural rubber. *J. Mech. Phys. Solids* **116**, 350-369, doi:10.1016/j.jmps.2018.04.003 (2018).

30 Plagge, J. & Kluppel, M. A Theory Relating Crystal Size, Mechanical Response, and Degree of Crystallization in Strained Natural Rubber. *Macromolecules* **51**, 3711-3721, doi:10.1021/acs.macromol.8b00177 (2018).

31 Gros, A., Huneau, B., Verron, E. & Tosaka, M. A physically-based model for strain-induced crystallization in natural rubber. Part I: Life cycle of a crystallite. *J. Mech. Phys. Solids* **125**, 164-177, doi:10.1016/j.jmps.2018.12.011 (2019).

32 Gros, A., Verron, E. & Huneau, B. A physically-based model for strain-induced crystallization in natural rubber. Part II: Derivation of the mechanical model. *J. Mech. Phys. Solids* **125**, 255-275, doi:10.1016/j.jmps.2018.12.014 (2019).

33 Dargazany, R., Khiem, V. N., Poshtan, E. A. & Itskov, M. Constitutive modeling of strain-induced crystallization in filled rubbers. *Physical Review E* **89**, 022604, doi:ARTN 022604, 10.1103/PhysRevE.89.022604 (2014).

34 Baumgartner, R. *et al.* A Lesson from Plants: High-Speed Soft Robotic Actuators. *Adv. Sci.* **7**, 1903391, doi:ARTN 1903391, 10.1002/advs.201903391 (2020).

35 Mullins, L. Softening of rubber by deformation. *Rubber Chem. Technol.* **42**, 339-362 (1969).

36 Treloar, L. R. G. *The physics of rubber elasticity*. 3rd edn, (Clarendon Press, 2005).

37 Holzapfel, G. A. *Nonlinear solid mechanics : a continuum approach for engineering*. (Wiley, 2000).

38 Volokh, K. Y. *Mechanics of soft materials*. (Springer Berlin Heidelberg, 2016).

39 Fung, Y. C. *Biomechanics : mechanical properties of living tissues*. 2nd edn, (Springer-Verlag, 1993).

40 Tschoegl, N. W. *The phenomenological theory of linear viscoelastic behavior : an introduction*. (Springer-Verlag, 1989).

41 Gutierrez-Lemini, D. *Engineering viscoelasticity*. (Springer, 2014).

42 De Pascalis, R., Abrahams, I. D. & Parnell, W. J. On nonlinear viscoelastic deformations: a reappraisal of Fung's quasi-linear viscoelastic model. *Proceedings of the Royal Society a-Mathematical Physical and Engineering Sciences* **470**, 20140058, doi:ARTN 20140058, 10.1098/rspa.2014.0058 (2014).

43 De Pascalis, R. *et al.* The inflation of viscoelastic balloons and hollow viscera. *Proceedings of the Royal Society a-Mathematical Physical and Engineering Sciences* **474**, 20180102, doi:ARTN 20180102, 10.1098/rspa.2018.0102 (2018).

44 Ruellan, B. *et al.* Fatigue crack growth in natural rubber: The role of SIC investigated through post-mortem analysis of fatigue striations. *Eng. Fract. Mech.* **201**, 353-365, doi:10.1016/j.engfracmech.2018.07.001 (2018).

45 Ruellan, B. *et al.* Fatigue of natural rubber under different temperatures. *Int. J. Fatigue* **124**, 544-557, doi:10.1016/j.ijfatigue.2018.10.009 (2019).

46 Sebald, G., Xie, Z. J. & Guyomar, D. Fatigue effect of elastocaloric properties in natural rubber. *Philosophical Transactions of the Royal Society a-Mathematical Physical and Engineering Sciences* **374**, doi:10.1098/rsta.2015.0302 (2016).

47 Sebald, G., Komiya, A., Jay, J., Coativy, G. & Lebrun, L. Regenerative cooling using elastocaloric rubber: Analytical model and experiments. *J. Appl. Phys.* **127**, doi:10.1063/1.5132361 (2020).

48 Carslaw, H. S. & Jaeger, J. C. *Conduction of heat in solids*. 2nd edn, (Clarendon Press; Oxford University Press, 1986).

49 Landau, L. D. & Lifshit͡s, E. M. *Fluid mechanics*. 2nd edn, (Pergamon Press, 1987).

50 Bird, R. B., Stewart, W. E. & Lightfoot, E. N. *Transport Phenomena*. (Wiley, 2006).

51 VDI-Gesellschaft Verfahrenstechnik und Chemieingenieurwesen. *VDI heat atlas*. 2nd edn, (Springer, 2010).

52 Gao, Q. *et al.* Experimental investigation on refrigeration performance of a reciprocating active magnetic regenerator of room temperature magnetic refrigeration. *International Journal of Refrigeration* **29**, 1274-1285, doi:https://doi.org/10.1016/j.ijrefrig.2005.12.015 (2006).

53 Clot, P. *et al.* A magnet-based device for active magnetic regenerative refrigeration. *IEEE Transactions on Magnetics* **39**, 3349-3351, doi:10.1109/TMAG.2003.816253 (2003).

54 Zimm, C. *et al.* in *Advances in Cryogenic Engineering* (ed Peter Kittel) 1759-1766 (Springer US, 1998).

55 Aprea, C., Greco, A., Maiorino, A. & Masselli, C. The energy performances of a rotary permanent magnet magnetic refrigerator. *International Journal of Refrigeration* **61**, 1-11, doi:https://doi.org/10.1016/j.ijrefrig.2015.09.005 (2016).

56 Tura, A. & Rowe, A. Permanent magnet magnetic refrigerator design and experimental characterization. *International Journal of Refrigeration* **34**, 628-639, doi:https://doi.org/10.1016/j.ijrefrig.2010.12.009 (2011).

57 Lozano, J. A. *et al.* Performance analysis of a rotary active magnetic refrigerator. *Applied Energy* **111**, 669-680, doi:https://doi.org/10.1016/j.apenergy.2013.05.039 (2013).

58 Jacobs, S. *et al.* The performance of a large-scale rotary magnetic refrigerator. *International Journal of Refrigeration* **37**, 84-91, doi:https://doi.org/10.1016/j.ijrefrig.2013.09.025 (2014).

59 Li, B. *et al.* Colossal barocaloric effects in plastic crystals. *Nature* **567**, 506-510, doi:10.1038/s41586-019-1042-5 (2019).

60 Aznar, A. *et al.* Reversible and irreversible colossal barocaloric effects in plastic crystals. *Journal of Materials Chemistry A* **8**, 639-647, doi:10.1039/C9TA10947A (2020).

61 Carvalho, A. M. G., Imamura, W., Usuda, E. O. & Bom, N. M. Giant room-temperature barocaloric effects in PDMS rubber at low pressures. *European Polymer Journal* **99**, 212-221, doi:https://doi.org/10.1016/j.eurpolymj.2017.12.007 (2018).

62 Defay, E. *et al.* Enhanced electrocaloric efficiency via energy recovery. *Nature Communications* **9**, 1827, doi:10.1038/s41467-018-04027-9 (2018).

63 Wang, Y. *et al.* A high-performance solid-state electrocaloric cooling system. *Science* **370**, 129-133, doi:10.1126/science.aba2648 (2020).

64 Torelló, A. *et al.* Giant temperature span in electrocaloric regenerator. *Science* **370**, 125-129, doi:10.1126/science.abb8045 (2020).

65 Li, Y. *et al.* Energy-Efficient Elastocaloric Cooling by Flexibly and Reversibly Transferring Interface in Magnetic Shape-Memory Alloys. *ACS Applied Materials & Interfaces* **10**, 25438-25445, doi:10.1021/acsami.8b07703 (2018).

66 Engelbrecht, K. *et al.* A regenerative elastocaloric device: experimental results. *Journal of Physics D: Applied Physics* **50**, 424006, doi:10.1088/1361-6463/aa8656 (2017).

67 Porenta, L. *et al.* Thin-walled Ni-Ti tubes under compression: ideal candidates for efficient and fatigue-resistant elastocaloric cooling. *Applied Materials Today* **20**, 100712, doi:https://doi.org/10.1016/j.apmt.2020.100712 (2020).

68 Wang, R. *et al.* Torsional refrigeration by twisted, coiled, and supercoiled fibers. *Science* **366**, 216-221, doi:10.1126/science.aax6182 (2019).

69 Snodgrass, R. & Erickson, D. A multistage elastocaloric refrigerator and heat pump with 28 K temperature span. *Scientific Reports* **9**, 18532, doi:10.1038/s41598-019-54411-8 (2019).

70 Tušek, J. *et al.* A regenerative elastocaloric heat pump. *Nature Energy* **1**, 16134, doi:10.1038/nenergy.2016.134 (2016).

71 Ma, R. *et al.* Highly efficient electrocaloric cooling with electrostatic actuation. *Science* **357**, 1130-1134, doi:10.1126/science.aan5980 (2017).

72 Ossmer, H. *et al.* Energy-efficient miniature-scale heat pumping based on shape memory alloys. *Smart Materials and Structures* **25**, 085037, doi:10.1088/0964-1726/25/8/085037 (2016).

73 Bruederlin, F., Ossmer, H., Wendler, F., Miyazaki, S. & Kohl, M. SMA foil-based elastocaloric cooling: from material behavior to device engineering. *Journal of Physics D: Applied Physics* **50**, 424003, doi:10.1088/1361-6463/aa87a2 (2017).

74 Bruederlin, F. *et al.* Elastocaloric Cooling on the Miniature Scale: A Review on Materials and Device Engineering. *Energy Technology* **6**, 1588-1604, doi:10.1002/ente.201800137 (2018).